

Aberystwyth University

'Structure-from-Motion' photogrammetry: A low-cost, effective tool for geoscience applications

Westoby, M. J.; Brasington, J.; Glasser, N. F.; Hambrey, M. J.; Reynolds, J. M.

Published in:
Geomorphology

DOI:
[10.1016/j.geomorph.2012.08.021](https://doi.org/10.1016/j.geomorph.2012.08.021)

Publication date:
2012

Citation for published version (APA):

Westoby, M. J., Brasington, J., Glasser, N. F., Hambrey, M. J., & Reynolds, J. M. (2012). 'Structure-from-Motion' photogrammetry: A low-cost, effective tool for geoscience applications. *Geomorphology*, 179, 300-314. <https://doi.org/10.1016/j.geomorph.2012.08.021>

General rights

Copyright and moral rights for the publications made accessible in the Aberystwyth Research Portal (the Institutional Repository) are retained by the authors and/or other copyright owners and it is a condition of accessing publications that users recognise and abide by the legal requirements associated with these rights.

- Users may download and print one copy of any publication from the Aberystwyth Research Portal for the purpose of private study or research.
- You may not further distribute the material or use it for any profit-making activity or commercial gain
- You may freely distribute the URL identifying the publication in the Aberystwyth Research Portal

Take down policy

If you believe that this document breaches copyright please contact us providing details, and we will remove access to the work immediately and investigate your claim.

tel: +44 1970 62 2400
email: is@aber.ac.uk

1 **'Structure-from-Motion' photogrammetry: a low-cost,** 2 **effective tool for geoscience applications**

3 M.J. Westoby^{1,*}, J. Brasington², N.F. Glasser¹, M.J. Hambrey¹, and J.M. Reynolds³

4
5 *Corresponding author. Tel.: +44 1970 628 608; Fax: +44 1970 622 659

6 E-mail: mjwestoby@gmail.com

7
8 ¹Institute of Geography and Earth Sciences, Penglais Campus, Aberystwyth University, UK

9 ²School of Geography, Queen Mary, University of London, London, UK

10 ³Reynolds International Ltd., Unit 17, Mold Business Park, Mold, UK.

11 12 **Abstract:**

13 High-resolution topographic surveying is traditionally associated with high capital and
14 logistical costs, so that data acquisition is often passed on to specialist third party
15 organizations. The high costs of data collection are, for many applications in the
16 earth sciences, exacerbated by the remoteness and inaccessibility of many field
17 sites, rendering cheaper, more portable surveying platforms (i.e. terrestrial laser
18 scanning or GPS) impractical. This paper outlines a revolutionary, low-cost, user-
19 friendly photogrammetric technique for obtaining high-resolution datasets at a range
20 of scales, termed 'Structure-from-Motion' (SfM). Traditional softcopy
21 photogrammetric methods require the 3-D location and pose of the camera(s), or the
22 3-D location of ground control points to be known to facilitate scene triangulation and
23 reconstruction. In contrast, the SfM method solves the camera pose and scene
24 geometry simultaneously and automatically, using a highly redundant bundle
25 adjustment based on matching features in multiple overlapping, offset images. A
26 comprehensive introduction to the technique is presented, followed by an outline of
27 the methods used to create high-resolution Digital Elevation Models (DEMs) from
28 extensive photosets obtained using a consumer-grade digital camera. As an initial
29 appraisal of the technique, an SfM-derived DEM is compared directly with a similar
30 model obtained using Terrestrial Laser Scanning. This intercomparison reveals that
31 decimetre-scale vertical accuracy can be achieved using SfM even for sites with
32 complex topography and a range of land-covers. Example applications of SfM are
33 presented for three contrasting landforms across a range of scales including; an
34 exposed rocky coastal cliff; a breached moraine-dam complex; and a glacially-
35 sculpted bedrock ridge. The SfM technique represents a major advancement in the
36 field of photogrammetry for geoscience applications. Our results and experiences
37 indicate SfM is an inexpensive, effective, and flexible approach to capturing complex
38 topography.

39 **Key words:**

40 Structure-from-Motion; SfM; Close- range photogrammetry; Digital Elevation Model

41 1. Introduction

42 The last decade has witnessed a technological revolution in geomatics that is
43 transforming digital elevation modelling and geomorphological terrain analysis.
44 Spurred on by developments in traditional ground surveying, such as the advent of
45 differential GPS (e.g., Brasington et al., 2000) and reflectorless, robotic total stations
46 (e.g. Keim et al., 1999; Fuller et al., 2003), the acquisition of topographic data has
47 been transformed most significantly by a new generation of remote sensing
48 technologies. Airborne and more recently terrestrial laser scanning (e.g., Lohani and
49 Mason, 2001; Jones et al., 2007; Notebaert et al., 2009; Rosser et al., 2005;
50 Heritage and Hetherington, 2007; Hodge et al., 2009) and soft-copy photogrammetry
51 (e.g., Lane et al., 2000; Westaway et al., 2000; Brasington et al., 2003) in particular,
52 have revolutionized the quality of DEMs, extending their spatial extent, resolution,
53 and accuracy.

54 Developments in airborne and terrestrial remote sensing have also been mirrored by
55 advances in hydrographic surveying, in particular through single and multi-beam
56 sonar (e.g., Parsons et al., 2005; Sacchetti et al., 2012). These acoustic soundings,
57 capable of centimetric data spacing and 3-D point quality herald the potential to
58 construct truly continuous, high fidelity terrain models of mixed terrestrial, freshwater
59 and marine environments. Finally, and closing the technological loop, the acquisition
60 of remotely sensed data from a range of cheap, lightweight platforms on which to
61 deploy imaging sensors, such as unmanned aerial vehicles or UAVs (e.g., Lejot et al.
62 2007; Niethammer et al., 2012) and tethered kites and blimps (e.g., Marzloff et al.,
63 2003; Boike and Yoshikawa, 2003; Smith et al., 2009; Vericat et al., 2009,) is
64 gradually becoming more commonplace.

65 While the pace of development in geospatial technologies has been rapid, the
66 acquisition of high quality terrain data nonetheless remains challenging in remote,
67 high alpine environments. In these hostile landscapes, steep and unconsolidated
68 slopes and poor satellite coverage hinders the application of ground surveys by GPS
69 or total station. Alternative ground-based methods such as terrestrial laser scanning
70 (TLS) are complicated by the high capital investment cost and the portability of large
71 instruments and their power requirements in remote areas. Airborne surveys,
72 including LiDAR and photography are also of restricted use due to the high three-
73 dimensionality of mountainous landscapes, which results in significant line of sight
74 losses and image foreshortening. Moreover, deploying survey platforms, including
75 helicopters and smaller scale UAVs at altitude is highly dependent on favourable
76 weather conditions and may often be hampered by high wind speed and cloud cover.
77 Potential solutions may ultimately lie in the availability of high resolution satellite
78 data, but at present the spatial resolution of the majority of existing active and
79 passive sensors is typically too coarse to create digital elevation models (DEMs) at
80 resolutions comparable to ground-based techniques and suitable for detailed
81 geomorphological applications

83 **1.1. Photogrammetric Survey Methods**

84 In the decade or so since its emergence, automated aerial and close-range digital
85 photogrammetry has become a powerful and widely used tool for three-dimensional
86 topographic modelling (Remondino and El-Hakim, 2006; Matthews, 2008). The
87 development of soft-copy triangulation and image-based terrain extraction algorithms
88 have radically enhanced the quality of terrain data that can be derived from
89 overlapping stereo-pairs (Chandler, 1999; Lane et al., 2000). Similarly,
90 improvements in the cost and quality of compact and single lens reflex (SLR)
91 cameras, and methods for the calibration of such non-metric cameras (Clarke and
92 Fryer, 1998; Chandler et al., 2005) have democratized access to photogrammetric
93 modelling and encouraged a wide range of uses in geomorphology. This has
94 included monitoring river bed topography and planform (e.g. Lane, 2000; Chandler et
95 al., 2002; Brasington and Smart, 2003; Bird et al., 2010), river bank (e.g. Barker et
96 al., 1997; Pyle et al., 1997) and gully erosion (e.g. Betts and DeRose, 1999; Marzloff
97 and Poesen, 2010), and in the field of glaciology, the quantification of glacier surface
98 change (e.g. Keutterling and Thomas, 2006; Baltsavias et al., 2008). Digital
99 photogrammetry has also been applied to a number of geological problems,
100 including discontinuity characterization (e.g. Krosley et al., 2006; Sturzenegger and
101 Stead, 2009) and rock slope stability analysis (e.g. Haneberg, 2008). Close-range
102 applications have also included direct quantification of soil erosion and the
103 morphodynamics of laboratory-scale landscape evolution models (e.g. Stojic et al.,
104 1998; Brasington and Smart, 2003; Lane et al., 2001; Hancock and Willgoose, 2001;
105 Rieke-Zapp and Nearing, 2005; Heng et al., 2010).

106

107 **1.2. Structure-from-Motion**

108 In this paper, we report on an emerging, low-cost photogrammetric method for high
109 resolution topographic reconstruction, ideally suited for low-budget research and
110 application in remote areas. 'Structure-from-Motion' (SfM) operates under the same
111 basic tenets as stereoscopic photogrammetry, namely that 3-D structure can be
112 resolved from a series of overlapping, offset images (Fig. 1). However, it differs
113 fundamentally from conventional photogrammetry, in that the geometry of the scene,
114 camera positions and orientation are solved automatically without the need to specify
115 *a priori*, a network of targets which have known 3-D positions. Instead, these are
116 solved simultaneously using a highly redundant, iterative bundle adjustment
117 procedure, based on a database of features automatically extracted from a set of
118 multiple overlapping images (Snavely, 2008). As described below, the approach is
119 most suited to sets of images with a high degree of overlap that capture full three-
120 dimensional structure of the scene viewed from a wide array of positions, or as the
121 name suggests, images derived from a moving sensor.

122 Developed in the 1990s, this technique has its origins in the computer vision
123 community (e.g. Spetsakis and Aloimonos, 1991; Boufama et al., 1993; Szeliski and
124 Kang, 1994) and the development of automatic feature-matching algorithms in the
125 previous decade (e.g. Förstner, 1986; Harris and Stephens, 1988). The approach
126 has been popularized through a range of cloud-processing engines, most notably
127 Microsoft® Photosynth™ (Microsoft, 2010), which uses SfM approaches
128 documented in Snavely (2008) and Snavely *et al.* (2008). These tools can make
129 direct use of user-uploaded and crowd-sourced photography to generate the
130 necessary coverage of a target scene, and can automatically generate sparse 3-D
131 point clouds from these photosets. The possibilities of SfM appear boundless,
132 however, to date, the technique has rarely been used within the geosciences (e.g.
133 Niethammer et al., 2012) and there exist few quantitative assessments of the quality
134 of terrain products derived from this approach.

135

136 **1.3. The First Principles of SfM**

137 To determine the 3-D location of points within a scene, traditional softcopy
138 photogrammetric methods require the 3-D location and pose of the camera(s), or the
139 3-D location of a series of control points to be known. Using the former, in the
140 absence of a camera-mounted GPS and electronic compass, triangulation can be
141 used to reconstruct scene geometry, whilst in the case of the latter, control points are
142 manually identified in the input photographs, and a process called *resectioning*, or
143 *camera pose estimation*, used to determine camera position. In contrast, the SfM
144 approach requires neither of the above to be known prior to scene reconstruction.
145 Camera pose and scene geometry are reconstructed simultaneously through the
146 automatic identification of matching features in multiple images. These features are
147 tracked from image to image, enabling initial estimates of camera positions and
148 object coordinates which are then refined iteratively using non-linear least-squares
149 minimization (as multiple solutions become available from the wide range of features
150 in the image database (Snavely, 2008)).

151 Unlike traditional photogrammetry, the camera positions derived from SfM lack the
152 scale and orientation provided by ground-control coordinates. Consequently, the 3-
153 D point clouds are generated in a relative 'image-space' coordinate system, which
154 must be aligned to a real-world, 'object-space' co-ordinate system. In most cases,
155 the transformation of SfM image-space coordinates to an absolute coordinate
156 system can be achieved using a 3-D similarity transform based on a small number of
157 known ground-control points (GCPs) with known object-space coordinates. Such
158 GCPs can be derived post-hoc, identifying candidate features clearly visible in both
159 the resulting point cloud and in the field, and obtaining their coordinates by ground
160 survey (i.e., by GPS). In practice, however, it is often easier to deploy physical
161 targets with a high contrast and clearly defined centroid in the field before acquiring
162 images. This approach simplifies the unambiguous co-location of image and object

163 space targets and also ensures a reliable, well-distributed network of targets across
164 the area of interest, enabling an assessment of any non-linear structural errors in the
165 SfM reconstruction. It is also useful to incorporate a degree of redundancy in the
166 GCP network to counter the possibility of sparse data in the region of the targets.

167

168 **1.4. Goals of this Article**

169 The aim of this paper is to provide an introduction to SfM and a detailed explanation
170 of the methods employed; illustrating the steps required to generate a fully rendered
171 3-D model, starting from the initial acquisition of the photographic data. The focus
172 here is to outline a practical workflow that could be applied by environmental
173 scientists and practitioners interested in deploying SfM for geomorphological
174 research. To achieve this, we describe a workflow that uses the freely available
175 application bundle SFMToolkit3 (Astre, 2010) to process the photographs and
176 produce the initial point cloud. This package contains a number of open-source
177 applications including, in order of execution, SiftGPU (Lowe, 1999, 2004), Bundler
178 (Snavely et al., 2008), CMVS and PMVS2 (Furukawa and Ponce, 2007; Furukawa et
179 al., 2010), all of which may be run independently if desired.

180 Applications of SfM to a range of contrasting landscapes and landforms are
181 described, including coastal cliffs, a moraine-dammed lake, and a smaller scale
182 glacially-sculpted bedrock ridge. Importantly, we also undertake a detailed
183 assessment of the quality of a derived topographic model, in this case a c. 300 x 300
184 m cliff section in Aberystwyth, Wales, through comparison with a high resolution
185 terrain model derived from a precision terrestrial laser scan survey.

186

187 **2. Method**

188

189 **2.1. Structure-from-Motion workflow**

190

191 **2.1.1. Image acquisition and keypoint extraction**

192 The key problem that SfM addresses is the determination of the 3-D location of
193 matching features in multiple photographs, taken from different angles. The initial
194 processing step in the solution of this problem is the identification of features in
195 individual images which may be used for image correspondence. A popular solution
196 to this, and used in the methods popularized by Snavely (2008) is the Scale Invariant
197 Feature Transform (SIFT) object recognition system. This is implemented in
198 SFMToolkit3, through the incorporation of the SiftGPU algorithm (Lowe, 1999; 2004).

199

200 This identifies features in each image that are invariant to the image scaling and
201 rotation and partially invariant to changes in illumination conditions and 3-D camera
202 viewpoint (Fig. 2; Lowe, 2004). Points of interest, or 'keypoints', are automatically
203 identified over all scales and locations in each image, followed by the creation of a
204 feature descriptor, computed by transforming local image gradients into a
205 representation that is largely insensitive to variations in illumination and orientation
206 (Lowe, 2004). These descriptors are unique enough to allow features to be matched
207 in large datasets.

208 The number of keypoints in an image is dependent primarily on image texture and
209 resolution, such that complex images at high (often original) resolutions will return
210 the most results. The density, sharpness, and resolution of the photoset, combined
211 with the range of natural scene textures will, in the first instance therefore, determine
212 the quality of the output point cloud data. Similarly, decreasing the distance between
213 the camera and feature of interest, thereby increasing the spatial resolution of the
214 photograph, will enhance the spatial density and resolution of the final point cloud.

215 Variations in the complexity, lighting, materials in individual scenes all influence the
216 image texture so it is impossible to offer explicit guidance on the minimum number of
217 photographs necessary for successful scene reconstruction. The minimum
218 requirement is for corresponding features to be visible in a minimum of three
219 photographs, however, obtaining as many images for SfM input as possible, given
220 logistical constraints, is highly recommended as this optimizes the ultimate number
221 of keypoint matches and system redundancy.

222 Particular consideration should also be given to the choice of acquisition platform.
223 For example, small scale sites with steep slope angles are likely to be better suited
224 to an exclusively ground-based approach, whereas low altitude aerial photography
225 (LAAP) may provide better coverage over larger sites and those with more subdued
226 topography. Indeed, imagery combined from multiple platforms may prove to be
227 optimal, providing different levels of detail in different areas of the scene. When
228 acquiring the photographs, particular attention should be taken to maximise overlap
229 by adopting short camera baselines (i.e., the distance between successive
230 photography positions), and obtaining as uniform coverage of the feature or
231 landscape of interest as possible.

232 A wide variety of imaging sensors can be used for SfM, from video stills, through to
233 low grade compact digital cameras. The primary requirement is well-exposed
234 photographs of the feature(s) of interest. From our experience, 'bigger' is not
235 necessarily 'better'. Whereas image quality and resolution are improved by using
236 increasingly expensive digital SLR models, images captured at the highest
237 resolutions (e.g. >12 megapixel) will almost inevitably need to be re-sized (with the
238 consequent loss of image detail) to avoid lengthy processing times. If operating in
239 remote regions, specific consideration should be given to robustness and battery life,
240 including methods for charging and performance in extreme temperatures.

241

242 **2.1.2. 3-D scene reconstruction**

243 Following keypoint identification and descriptor assignment, the sparse bundle
244 adjustment system Bundler (Snavely et al., 2008) is used to estimate camera pose
245 and extract a low-density or 'sparse' point cloud. Keypoints in multiple images are
246 matched using approximate nearest neighbour (Arya et al., 1998) and Random
247 Sample Consensus (RANSAC; Fischler and Bolles, 1987) algorithms, and 'tracks'
248 linking specific keypoints in a set of pictures, are established. Tracks comprising a
249 minimum of two keypoints and three images are used for point-cloud reconstruction,
250 with those which fail to meet these criteria being automatically discarded (Snavely et
251 al., 2006). Using this method, transient features such as people moving across the
252 area of interest are automatically removed from the dataset before 3-D
253 reconstruction begins. This also applies to non-static objects unintentionally captured
254 in the input photoset, such as objects on the sensor, blimp or kite tethers, or
255 helicopter landing skids. In these instances, although identical keypoints referencing
256 such objects will be created, they are not suitable for use in scene reconstruction as
257 their position relative to other keypoints is constantly changing, and are automatically
258 filtered using visibility and regularization constraints (Furukawa and Ponce, 2009).

259 Keypoint correspondences place constraints on camera pose orientation, which is
260 reconstructed using a similarity transformation, while minimization of errors is
261 achieved using a non-linear least-squares solution (Szeliski and Kang, 1994;
262 Nocedal and Wright, 1999). Finally, triangulation is used to estimate the 3-D point
263 positions and incrementally reconstruct scene geometry, fixed into a relative
264 coordinate system. Full automation of this process, from keypoint extraction, to
265 accurate reconstruction of scene geometry is a clear advantage of the SfM method
266 over traditional digital photogrammetric approaches.

267 The bundle adjustment package used in Bundler (Lourakis and Argyros, 2009)
268 produces sparse point-clouds. An enhanced density point-cloud can be derived by
269 implementing the Clustering View for Multi-view Stereo (CMVS) (Furukawa and
270 Ponce, 2007; Furukawa et al., 2010) and Patch-based Multi-view Stereo (PMVS2)
271 algorithms (Furukawa and Ponce, 2007). Here, camera positions derived from
272 Bundler are used as input. CMVS then decomposes overlapping input images into
273 subsets or clusters of manageable size, whilst PMVS2 is used to independently
274 reconstruct 3-D data from these individual clusters (Furukawa and Ponce, 2007).
275 The result of this additional processing is a significant increase in point density;
276 typically approaching, or in excess of 2 orders of magnitude (Table 1).

277

278 **2.1.3. Post-processing and digital elevation model generation**

279 Transformation from a relative to absolute co-ordinate system is achieved through
280 manual identification of GCPs in the point cloud and the computation of an

281 appropriate transformation. Here, we use a rigid body transformation decomposed
282 into a rotation and a translation matrix, and a scale factor. A solution to this
283 transformation is found using a modified version of Horn's (1987) absolute
284 orientation algorithm implemented in MATLAB®. A solution to the seven unknowns
285 in the total transformation requires a minimum of three matching image and object
286 space coordinates.

287 Targets are placed to provide maximum visibility (and thus obvious appearance in
288 the photographs), and contrast as strongly as possible with the surroundings to aid
289 their location in the final point-cloud before the data are transformed. Significant
290 outliers and artefacts (e.g. erroneous peaks and troughs resulting from keypoint
291 descriptor mismatches) and any unnecessarily reconstructed surrounding
292 topography are manually removed at this stage.

293 The point clouds generated using SfM may, depending on the image set, be
294 extremely dense, potentially incorporating upwards of 10^3 3-D points per square
295 metre. Direct interpolation of the raw point cloud into a typically coarser resolution
296 terrain model (e.g., metre-scale) represents a considerable computational task.
297 Additionally, and in common with other remote sensing methods such as LiDAR or
298 TLS, this raw point cloud may also incorporate 'off-ground' features that obscure
299 simple geomorphological interpretation.

300 To improve data-handling and provide a first-order bare-earth elevation model, here
301 we decimate the raw point cloud using a gridding procedure developed by Rychkov
302 et al. (2012). This approach, originally designed to explore TLS point clouds,
303 decomposes the point cloud into a regular grid, for which parameters of the local
304 elevation distribution are extracted. These include the minimum, maximum, mean
305 and first and higher order moments. The routine then fits a local tessellation to this
306 reduced resolution grid, based on a local elevation estimate, and then detrends the
307 raw point cloud, to derive a comparable set of local statistics that reflect variability
308 above the first order grid-scale features. This simple, but computationally efficient
309 procedure allows easy extraction of terrain models based, for example on the local
310 minimum grid elevation, whilst retaining information on the sub-grid elevation
311 complexity for later analysis. Visualisation of the grid-cell statistics also permits
312 spatial analysis of the variability in point density across the entire model (see Fig.
313 6d).

314 When combined, SfM and point-cloud decimation potentially offer a powerful tool for
315 geomorphological analysis. For example, using the approach on comparable TLS
316 derived point clouds, Rychkov et al. (2012) were able reveal gravel-scale grain scale
317 roughness on steeply inclined river banks. Similarly, in the absence of high-
318 resolution imagery from space-borne platforms or aerial LiDAR, entire floodplains
319 and valley floor reaches may be surveyed using cameras mounted on low-altitude
320 tethered platforms or UAVs (e.g. Niethammer, 2012) and subsequently decimated to

321 resolutions required for the extraction of geometric data required as boundary
322 condition data for hydrodynamic modelling.

323 However, depending on the final application, data decimation may not be necessary
324 and unwanted, although conventional GIS software is typically inappropriate to
325 manage the visualization and storage of dense point data which may extend into
326 tens or hundreds of millions of observations. For the examples presented in this
327 paper, decimation was applied in order to facilitate direct comparison of SfM and
328 TLS data at resolutions sufficient to represent the first order topography at the scale
329 of interest whilst enabling simple surface generation and visualisation on a desktop
330 PC. The final terrain products were derived by linearly resampling a TIN created by
331 Delaunay triangulation in ArcGIS from decimated point cloud (following, Brasington
332 et al., 2000). This model may be visualized effectively by draping the orthophoto
333 derived from the SfM processing over this surface. The final result is a fully
334 georeferenced, high-resolution, photo-realistic DEM. The complete workflow is
335 shown in Fig. 3.

336

337 **3. Comparison with Terrestrial Laser Scanning**

338

339 **3.1. Data acquisition and processing**

340 An independent assessment of the accuracy of the SfM method was undertaken by
341 direct comparison of raster DEMs of an exposed eroding cliff created using the SfM
342 workflow described above and a comparable survey with TLS. The study site is
343 Constitution Hill, a ~80 m high coastal cliff located immediately to the north of the
344 town of Aberystwyth, Wales, UK (Fig. 4a). The lower section of the cliff is
345 topographically complex, with land cover comprising grasses, shrubs, footpaths,
346 near-vertical cliff faces and rockfall debris. The exposed bedrock comprises Silurian
347 turbidites which were folded and faulted during the Caledonian orogeny. A cobble
348 beach is located at its base. Labelled yellow targets, 1 x 1 m in size were deployed
349 across the area of interest and used as GCPs. In total, 35 targets were distributed
350 across the study site, in a quasi-uniform pattern allowing for topographic constraints
351 (Fig. 4a).

352 In addition, three tripod-mounted Leica Geosystems HDS targets were deployed to
353 co-register the TLS data. Scans of the hillside were acquired from three positions
354 using a Leica Geosystems ScanStation (blue triangles in Fig. 4a). This was set to
355 record data with a 2 cm spatial resolution at a distance of 15 m for the first scan and
356 1 cm for the second and third. Coincidentally, a total of 889 photographs were taken
357 of the hillside using a consumer-grade digital camera (Panasonic DMC-G10, 12
358 megapixel resolution, with both automatic focusing and exposure enabled), from a
359 range of locations and perspectives, for use as input to SfM processing. Using three
360 people, TLS and SfM data acquisition, including deployment of the SfM GCPs (and

361 centroid location surveying) and TLS HDS targets, photograph acquisition, and TLS
362 data acquisition took approximately 5 hours in total, of which the SfM component
363 took approximately 2 hours. Total post-processing times were significantly longer:
364 combined, sparse and dense point cloud generation took a total of 23.5 hours, whilst
365 manual point cloud editing, GCP identification and transformation and DEM
366 generation took an additional ~4 hours.

367 The TLS data were co-registered into a single point cloud using a 3-D similarity
368 transformation based on manual identification of the three HDS targets in the
369 individual point-clouds. This was implemented using Leica's Cyclone software suite.
370 No attempt to transform the final product into an absolute coordinate system was
371 attempted, as this would incorporate additional unnecessary errors. The data were
372 also not projected, to allow a direct comparison of the two (TLS and SfM) matching
373 Cartesian coordinate systems.

374 The extensive photoset was decomposed into three 'batches' to reduce
375 computational demand, and input photographs re-scaled to 55% of their original
376 resolution to reduce computational demand. The processing steps outlined in section
377 2 were employed, producing unreferenced sparse and dense point-clouds as output
378 (Table 2). The SfM data were transformed to the TLS co-ordinate system through
379 manual identification of matching GCP centroids in both datasets (Fig. 4b-d). The
380 three SfM batches were registered individually, with no significant difference in the
381 quality of the three transformation models, and average transformation residuals of
382 0.124 m, 0.058 m and 0.031 m for xyz.

383

384 **3.2. Results**

385 Perspective views of the sparse and dense point cloud data are presented in Fig. 5.
386 A significant increase in the point density is immediately apparent for the dense
387 reconstruction. After manual editing, the sparse dataset comprised 1.7×10^5 points,
388 whilst the dense reconstruction produced 11.3×10^6 points; a 64-fold increase. This
389 is comparable to the TLS survey density with 11.7×10^6 survey points over the
390 same area. The resolution is sufficient to reveal bedrock structure, notably the style
391 of folding (Fig. 6, 'C' in Fig 5a).

392 Interpolated DEMs derived using the workflow described in Section 2 are shown in
393 Fig. 7. The models shown here have been extracted at 1 m resolution, and are
394 based on the local minimum elevation in order to aid the automatic removal any off-
395 ground observations (e.g., vegetation cover). The decimation process reduced the
396 original number of points to a regularised grid of 8999 and 10,780 cells for the SfM
397 and TLS data, whilst retaining key summary statistics describing the sub-grid
398 elevation variability.

399 There are minor differences in the spatial extent of the two models, though both
400 resolve clearly notable topographic elements such as near-vertical faces adjacent to
401 the main footpath (labelled 'A' and 'B' in Fig. 5a and Fig. 7a). Point density data (Fig.
402 7d, also Fig. 8) reveal that the highest concentrations (~70,000 - >90,000 points per
403 m²) are located towards the centre-north of the scene, corresponding to sizeable (up
404 to 10 m high) exposed rock faces.

405 A DEM of difference (DoD) was created by subtracting SfM elevation model from
406 that obtained by TLS (Fig. 9a). This reveals that 94 % of overlapping model
407 differences are in the range -1.0 – 1.0 m, with 86 % between just -0.5 – 0.5 m (Fig.
408 9b). Spatially, positive differences (SfM higher than TLS) in elevation are
409 concentrated towards the north-east of the dataset, with more pronounced negative
410 disparities confined largely to the west. The negative deviations correspond to the
411 headwall at the highest point of the scene, and steep faces which terminate at the
412 beach, respectively ('A' and 'B' in Fig. 7a, respectively).

413 It is hypothesized that the largest DoD values (Fig. 9a), corresponding to areas of
414 steeply sloping relief close to the beach and the headwall at the highest point of the
415 datasets, may be partly attributed to weak reconstruction caused by large camera-to-
416 feature baselines (>20 m) owing to the inaccessibility of these areas. The
417 photogrammetric-TLS model comparison in these areas is also likely to be highly
418 sensitive to small horizontal offsets introduced through point-cloud transformation.
419 Across the rest of the study area, it was possible to photograph the terrain from
420 relatively close proximity, including other steep areas which were well reconstructed,
421 as indicated by low Z_{diff} values (e.g., the centre of the study area, adjacent to the
422 footpath).

423 No statistically significant relationship ($r^2 = 0.19$) between slope and Z_{diff} exists,
424 suggesting that DEM disparities cannot be explained by the local gradient alone. The
425 areas with the highest differences were concentrated, almost exclusively, to the cliff
426 section adjacent to the beach in the west of the dataset ('B' in Fig. 8a) and
427 correspond to regions subjected to heavy interpolation. Dense vegetation dominates
428 the eastern end of Constitution Hill ('C' in Fig. 8a) this is strongly associated with
429 moderately high (positive) elevation differences. If comprehensive photosets with
430 high degrees of overlap are not acquired for this type of land cover, dense vegetation
431 cover proves problematic for effective terrain reconstruction due to the
432 homogeneous image texture. The same also applies to surfaces including grass,
433 snow, or sand.

434 The scale of elevation differences apparent between the two models appears to
435 imply that application of repeat SfM to monitor landscape change (by DEMs of
436 difference) would be limited to capturing only relatively large topographic dynamics
437 (i.e., metre scale). However, on closer inspection it is apparent that the notable local
438 deviations between the SfM and TLS datasets correspond largely to areas of
439 relatively dense shrub and bush cover. Indeed, considerably lower deviations (i.e. \pm

440 0.1 m or less) are found in the mostly vegetation-free (with the exception of short
441 grass) central portion of the site closest to the beach. To illustrate this point, Z_{diff}
442 frequency distribution histograms for two sub-regions of the site (both 20 m² in area),
443 representing an area of dense vegetation and largely vegetation-free ground,
444 respectively, are shown in Fig. 10. Analysis of these data reveal that 100% of cells
445 fall with the range -0.5 – 0.5 m for the vegetation-free region, with 89% of cells falling
446 within this classification for the area of dense vegetation. At the decimetre scale and
447 below, 61% and 39% of the vegetation-free and dense vegetation data, respectively,
448 possess Z_{diff} values of ± 0.1 m or less, demonstrating an appreciable decrease in
449 elevation difference in the absence of any significant vegetation cover. Error
450 introduced by the presence of vegetation is not an issue unique to the SfM method,
451 but may confound topographic reconstruction using a wide range of remote
452 surveying methods (e.g. Coveney and Fotheringham, 2011). Despite this, the
453 accuracy assessment serves as an encouraging first appraisal of the SfM algorithms
454 employed. A far more rigorous accuracy assessment, across a range of terrain
455 types, is needed in future research to better elucidate the major sources of error.
456 Similarly, a detailed investigation of systematic errors introduced by, for example, the
457 manual identification of the GCPs in both point cloud datasets, and the subsequent
458 impact upon the accuracy of the transformation matrix applied to the data, would
459 also be desirable.

460

461 **4. Applications of Structure-from-Motion to large- and small-** 462 **scale glacial landform reconstruction**

463

464 **4.1 Dig Tsho moraine complex**

465 The workflow outlined above was applied to the Dig Tsho moraine-dam complex in
466 the Khumbu Himal, Nepal (4,400 m) (Fig. 11a). Located at the head of the
467 Langmoche valley, the moraine dam failed on 4th August 1985 when an ice
468 avalanche from the receding Langmoche Glacier produced a displacement-wave
469 that overtopped the moraine dam and triggered its failure. The resulting glacial lake
470 outburst flood (GLOF) killed five people, livestock, and destroyed valuable arable
471 land as well as a newly-completed hydro-electric power plant (Vuichard and
472 Zimmerman, 1986, 1987; Richardson and Reynolds, 2000). The terminal moraine is
473 composed of a non-cohesive arrangement of locally-transported gravel, cobble, and
474 boulder-sized debris, and measures approximately 650 m wide and 80 m high at its
475 highest point. A sizeable breach, which measures ~40 m high and ~70 m across at
476 its widest point, dissects the northern edge of the terminal moraine.

477 Following the approach detailed above, a network of 35 GCPs was established
478 across the terminal moraine complex (Fig. 11b), and a set of 1649 photographs
479 taken from various locations and perspectives across the site. With a team of three
480 people, GCP deployment took approximately 10 hours due to the challenging

481 topography and effects of working at high altitude, whilst photograph acquisition was
482 completed in a little over 4 hours.

483 Feature matching and sparse bundle adjustment on three image batches ($n = 457$,
484 560 , and 609 images apiece) produced a total of 2.2×10^4 points, which, after dense
485 reconstruction and manual editing was increased to 13.2×10^6 . The SfM processing
486 took approximately 22 hours per batch, though access to a number of identical
487 machines allowed batches to be processed in tandem. The data were then geo-
488 registered and decimated gridded terrain products derived (producing a final grid of
489 $\sim 3.5 \times 10^5$ cells). GPS errors and transformation residuals are shown in Table 2. The
490 final, fully georeferenced DEM is displayed in Fig. 12a.

491 Although the focus of photograph-acquisition was the terminal moraine and breach,
492 background photographic information was sufficient to reconstruct the entire lake
493 basin, including the 2 km long northern lateral moraine. As in the previous example,
494 significant topographic detail (sub-metre scale) has been resolved. The entire
495 breach was successfully reconstructed, and notable morphological features captured
496 by the model include the narrow central section and expansive exit, as well as two
497 abandoned spillways. Highest point densities are concentrated along the inner faces
498 of the breach (where densities in excess of $>8,700$ points per m^2 may be found,
499 compared to a site-wide median of 7.35 per m^2 ; see also Fig. 8c), the eastern limit of
500 the distal face of the northern moraine, as well as the southern face of the relict
501 medial moraine which dissects the terminal moraine complex (Fig. 12b). A number of
502 interpolation artefacts are present across the scene, but are largely confined towards
503 the south and correspond to an extensive area of snow cover.

504

505 **4.2. Glacially-sculpted bedrock ridge, Cwm Cau**

506 Cwm Cau is a west-east orientated glacial cirque, located immediately to the south
507 of Cadair Idris (893 m) in Snowdonia National Park, Wales, UK (see Fig. 4a for
508 location). It is carved out of folded Ordovician volcanic rocks. A plethora of glacial
509 landforms are found inside the cirque and down-valley, including morainic
510 hummocks and ridges and glacially sculpted bedrock ridges (Sahlin and Glasser,
511 2008). The latter were deemed suitable for a small-scale appraisal of the SfM
512 technique. The bedrock ridge chosen for reconstruction is oriented west-east, is 80
513 m in length, 19 m across at its widest point, and approximately 6 m and 8 m high
514 along its southern and northern flanks, respectively (Fig. 13a). Twenty-two orange
515 targets measuring 0.1 m in diameter were used as GCPs. Given the scale of the
516 feature, a relative decrease in target size was deemed appropriate. Using dGPS,
517 horizontal, vertical, and combined positional accuracies of 0.002 m, 0.002 m, and
518 0.003 m were achieved. A total of 800 photographs were taken and used for scene
519 reconstruction. As in the previous example, SfM processing was performed on three
520 individual batches, taking an average of 12 hours each. Transformation residuals

521 averaged 0.975, 0.161, and 0.422 for x, y and z. Photograph and GCP data were
522 acquired at Cwm Cau in approximately 3 hours using two people, 1.5 hours of which
523 was spent establishing the GCP network.

524
525 The final interpolated DEM is shown in Fig. 13b and Fig. 14. Due to the smaller
526 scale of this feature, the point cloud was decimated to 10 cm spatial resolution,
527 reducing the original number of points from 8.9×10^6 to 1.3×10^5 . Analysis of
528 decimated cell statistics revealed an average point density of 69 per 0.1 m^2 (also Fig.
529 8d) providing outstanding detail of the feature's surface, particularly exposed, bare
530 rock faces found on the southern and northern flanks (Fig. 13b). Indeed, point
531 density on the southern face exceeded 90 points per 0.1 m^3 . This extreme
532 resolution is sufficient to delineate centimetre-scale bedrock joints and other surface
533 features such as striations. Scene reconstruction was weaker in topographically
534 complex and partially occluded regions such as the north-eastern edge of the feature
535 (see Fig. 14b), as a result of poorer photographic coverage and shadowing.

536

537 **5. Discussion**

538 As the above examples demonstrate, the apparent logistical advantages of SfM
539 (limited hardware needs and portability) are, at least in part, offset by the lengthy
540 processing times compared to 'data-ready' methods such as TLS or GPS. Keypoint
541 descriptor extraction, matching, and sparse and dense reconstruction algorithms are
542 computationally demanding. For example, total processing times for a typical
543 photoset used here, numbering between 400-600 images (at 2272×1740 pixel
544 resolution), range from 7-56 hours on a 64-bit system with a 2.8 GHz CPU, 512 MB
545 GPU and 6 GB RAM. This is heavily dependent on the complexity of image texture,
546 and may be ameliorated by reducing image size, although this will result in a
547 consequent decrease in the number of returned keypoint descriptors, and ultimately
548 reduced point density. Inevitably, the selection of SfM for any geoscience application
549 must take account of this significant post-processing load and the choice of survey
550 method will eventually be weighed against a number of factors, including cost,
551 accessibility, experience, and fitness-for-purpose in terms of data resolution and
552 coverage.

553 The sheer size of datasets generated using SfM, and for that matter those derived
554 from allied remote sensing methods such as TLS present significant information
555 management problems (Rychkov et al. 2012). The current generation of GIS are
556 largely inappropriate tools for this purpose, and the effective visualization and
557 analysis of high resolution point clouds is heavily constrained by the limited range of
558 software available for this purpose. The use of the point cloud decimation methods
559 described herein provide a useful strategy to down-scale these dense data whilst
560 retaining information concerning the sub-grid variability. However, while statistical

561 analysis of these decimated data may provide useful insights, for example to quantify
562 surface roughness, this step inevitably results in an unwanted loss of topographic
563 complexity. It is anticipated that future improvements in computational power will
564 reduce run times and facilitate the use of original, high-resolution photosets for input
565 to SfM processing, whilst the emergence of low-cost or freely-available software
566 products (e.g. MeshLab), capable of easily manipulating point clouds far in excess of
567 $>10^6$ of points will improve data handling and general accessibility to the approach.

568 The minimalistic nature of the approach also lends itself to aerial surveying.
569 Platforms including kites, lighter-than-air blimps and unmanned aerial vehicles
570 (UAVs) are equally portable, relatively inexpensive and capable of carrying both
571 basic and advanced photographic equipment (e.g. Smith et al., 2009; Vericat et al.,
572 2009; Niethammer et al., 2012), thereby vastly increasing the potential areal
573 coverage attained. In addition, aerial datasets have the potential to reduce, or even
574 eliminate the 'dead-ground' problem (Wolf and Dewitt, 2000), whereby objects in the
575 foreground of an image obscure those in the background, resulting in significant data
576 gaps. This issue applies not only to the SfM method, but to all point cloud acquisition
577 methods highly limited by line-of-sight. For topographically simple terrain, such as
578 outwash fans, and valley-floor floodplains, an aerial approach would be particular
579 advantageous. However, as with stereoscopic reconstruction, steep, or near-vertical
580 topography is likely to be problematic for the SfM technique. Further work is on-going
581 to appraise this approach.

582 The example applications presented in section 4 were ideally suited to the
583 application of the SfM technique. Minimal vegetation coverage and relatively
584 complex, heterogeneous topography at both the meso- and micro-scales facilitate
585 the extraction of suitable numbers of keypoint descriptors for consistent, dense point
586 cloud coverage. Similarly, the method is ideally suited for application in (semi)arid
587 environments. In contrast, the method's suitability for topographic reconstruction of,
588 for example, riparian landscapes may be limited, given that, at present, only water-
589 free surfaces would be suitable for reconstruction, and point density is likely to be
590 limited, and of questionable accuracy, in areas of dense vegetation.

591

592 **6. Conclusions**

593 This paper has outlined a novel low-cost, ground-based, close-range terrestrial
594 photogrammetry and computer vision approach to obtaining high-resolution spatial
595 data suitable for modelling meso- and micro-scale landforms. The nature of the SfM
596 method eliminates the requirement for manual identification of image control prior to
597 processing, instead employing automatic camera pose estimation algorithms to
598 simultaneously resolve 3-D camera location and scene geometry; this is an
599 extremely significant advantage of the technique over traditional digital
600 photogrammetric methods. However, as the raw SfM output is fixed into a relative

601 co-ordinate system, particular time and attention should be taken in the
602 establishment of a GCP network to facilitate transformation to an absolute co-
603 ordinate system and the extraction of metric data. Taking the hypothesised
604 effectiveness of an aerial approach into account, the terrestrial data collection
605 method presented herein nevertheless represents an effective, financially viable
606 alternative to traditional manual topographic surveying and photogrammetric
607 techniques, particularly for practical application in remote or inaccessible regions.

642 Brasington, J., Rumsby, B.T., McVey, R.A., 2000. Monitoring and modelling
643 morphological change in a braided gravel-bed river using high resolution GPS-based
644 survey. *Earth Surface Processes and Landforms* 25, 973-990.

645 Chandler, J.H., 1999. Effective application of automated digital photogrammetry for
646 geomorphological research. *Earth Surface Processes and Landforms* 24, 51-63.

647 Chandler, J.H., Ashmore, P., Paola, C., Gooch, M., Varkaris, F., 2002. Monitoring
648 river-channel change using terrestrial oblique digital imagery and automated digital
649 photogrammetry. *Annals of the Association of American Geographers* 92, 631-644.

650 Chandler, J.H., Fryer, J.G., Jack, A., 2005. Metric capabilities of low cost digital
651 cameras for close range surface measurement. *The Photogrammetric Record* 20,
652 12-26.

653 Clarke, T.A. and Fryer, J.G. 1998. The development of camera calibration methods
654 and models. *Photogrammetric Record*, 16, 51-66.

655 Coveney, S., Fotheringham, A.S. 2011. Terrestrial laser scan error in the presence
656 of dense ground vegetation. *The Photogrammetric Record* 26, 307-324.

657 Fischler, M.A., Bolles, R.C., 1987. Random Sample Consensus: a paradigm for
658 model fitting with applications to image analysis and automated cartography. In:
659 Martin, A.F., Oscar, F. (Eds.), *Readings in Computer Vision: Issues, Problems,*
660 *Principles, and Paradigms.* Morgan Kaufmann Publishers Inc., London, pp. 726-740.

661 Förstner, W., 1986. A feature-based correspondence algorithm for image matching.
662 *International Archives of Photogrammetry and Remote Sensing*, 26: 150-166.

663 Fraser, C.S., Cronk, S. 2009. A hybrid measurement approach for close-range
664 photogrammetry. *ISPRS Journal of Photogrammetry and Remote Sensing* 64, 328-
665 333.

666 Fuller I.C., Large, A.R.G., Milan, D., 2003. Quantifying channel development and
667 sediment transfer following chute cutoff in a wandering gravel-bed river.
668 *Geomorphology* 54, 307-323.

669 Furukawa, Y., Ponce, J., 2007. Accurate, dense, and robust multi-view stereopsis. In
670 *Proceedings, IEEE Conference on Computer Vision and Pattern Recognition*
671 *(CVPR)*, 17-22 June, Minneapolis, USA, 1-8.

672 Furukawa, Y., Curless, B., Seitz, M., Szeliski, R., 2010. Clustering view for multi-view
673 stereo. In *Proceedings, IEEE Conference on Computer Vision and Pattern*
674 *Recognition(CVPR)*, 13-18 June, San Francisco, USA, 1434-1441

675 Hancock, G.R., Willgoose, G.R., 2001. The production of digital elevation models for
676 experimental model landscapes. *Earth Surface Processes and Landforms* 26, 475-
677 490.

678 Haneberg, W.C., 2008. Using close range terrestrial digital photogrammetry for 3-D
679 rock slope modeling and discontinuity mapping in the United States. *Bulletin of*
680 *Engineering Geology and the Environment* 67, 457-469.

681 Harris, C., Stephens, M.. 1988. A combined corner and edge detector. *Proceedings*
682 *of the Fourth Alvey Vision Conference, Manchester*, 147-151.

683 Heng, B.C.P., Chandler, J.H., Armstrong, A., 2010. Applying close-range digital
684 photogrammetry and soil erosion studies. *The Photogrammetric Record* 25, 240-265.

685 Heritage, G., Hetherington, D., 2007. Towards a protocol for laser scanning in fluvial
686 geomorphology. *Earth Surface Processes and Landforms* 32, 66-74.

687 Hodge, R., Brasington, J., Richards, K., 2009. In-situ characterisation of grain-scale
688 fluvial morphology using Terrestrial Laser Scanning. *Earth Surface Processes and*
689 *Landforms* 34, 954-968.

690 Horn, B.K.P. 1987. Closed-form solution of absolute orientation using unit
691 quaternions. *Journal of the Optical Society of America* 4, 629-642.

692 Jones, A.F., Brewer, P.A., Johnstone, E., Macklin, M.G., 2007. High-resolution
693 interpretative geomorphological mapping of river valley environments using airborne
694 LiDAR data. *Earth Surface Processes and Landforms* 32, 1574-1592.

695 Keim, R.F., Skaugset, A.E., Bateman, D.S., 1999. Digital terrain modelling of small
696 stream channels with a total-station theodolite. *Advances in Water Resources* 23,
697 41-48.

698 Keutterling, A., Thomas, A., 2006. Monitoring glacier elevation and volume changes
699 with digital photogrammetry and GIS at Gepatschferner glacier, Austria. *International*
700 *Journal of Remote Sensing* 27, 4371-4380.

701 Krosley, L.K. Shaffner, P.T., Oerter, E., Ortiz, T., 2006. Digital ground-based
702 photogrammetry for measuring discontinuity orientations in steep rock exposures.
703 *Proceedings of the 41st U.S. Symposium of Rock Mechanics, Golden, Colorado*, pp.
704 1-13.

705 Lane, S.N., 2000. The measurement of river channel morphology using digital
706 photogrammetry. *The Photogrammetric Record* 16, 937-961.

707 Lane, S.N., James, T.D., Crowell, M.D., 2000. Application of digital photogrammetry
708 to complex topography for geomorphological research. *The Photogrammetric Record*
709 16, 793-821.

710 Lane, S.N., Chandler, J.H., Porfiri, K., 2001. Monitoring river channel and flume
711 surfaces with digital photogrammetry. *Journal of Hydraulic Engineering* 127, 871-
712 877.

713 Lejot, J., Delacourt, C., Piégay, H., Fournier, T., Trémélo, M-L., Allemand, P.,
714 2007. Very high spatial resolution imagery for channel bathymetry and topography
715 from an unmanned mapping controlled platform. *Earth Surface Processes and*
716 *Landforms* 32, 1705-1725.

717 Lohani, B., Mason, D.C., 2001. Application of airborne scanning laser altimetry to the
718 study of tidal channel geomorphology. *ISPRS Journal of Photogrammetry and*
719 *Remote Sensing* 56, 100-120.

720 Lourakis, M.I.A., Argyros, A.A., 2009. SBA: A software package for generic sparse
721 bundle adjustment. *ACM Transactions on Mathematical Software* 36: 1-30.

722 Lowe, D.G., 1999. Object recognition from local scale-invariant features,
723 *International Conference on Computer Vision, Corfu, Greece*, pp. 1150-1157.

724 Lowe, D., 2004. Distinctive image features from scale-invariant keypoints.
725 *International Journal of Computer Vision* 60, 91-110.

726 Marzoff, I., Poesen, J., 2009. The potential of 3-D gully monitoring with GIS using
727 high-resolution aerial photography and a digital photogrammetry system.
728 *Geomorphology* 111, 48-60.

729 Marzoff, I., Ries, J.B., Albert, K.D., 2002. Kite aerial photography for gully monitoring
730 in Sahelian landscapes . In *Proceedings of the Second Workshop of the EARSeL*
731 *Special Interest Group on Remote Sensing for Developing Countries*, 18-20
732 *September, Bonn, Germany*, 2-13.

733 Matthews, N.A., 2008. Aerial and close-range photogrammetric technology:
734 providing resource documentation, interpretation, and preservation. *Technical Note*
735 *428, Bureau of Land Management, Denver, Colorado*.

736 Microsoft®. 2010. Photosynth™. Available: <http://www.photosynth.net>.

737 Niethammer, U., James, M.R., Rothmund, S., Travelletti, J., Joswig, W., 2012. UAV-
738 based remote sensing of the Super Sauze landslide: Evaluation and results.
739 *Engineering Geology* 128, 2-11.

740 Nocedal, J., Wright, S.J., 1999. *Numerical optimization*. Springer: New York.

741 Notebaert, B., Verstraeten, G., Govers, G., Poesen, J., 2009. Qualitative and
742 quantitative applications of LiDAR imagery in fluvial geomorphology. *Earth Surface*
743 *Processes and Landforms* 34, 217-231.

744 Parsons, D. R., J. L. Best, O. Orfeo, R. J. Hardy, R. Kostaschuk, S. N. Lane., 2005.
745 Morphology and flow fields of three-dimensional dunes, Rio Paraná, Argentina:
746 Results from simultaneous multibeam echo sounding and acoustic Doppler current
747 profiling, *Journal of Geophysical Research*, 110, F04S03.

748 Pyle, C.J., Richards, K.S., Chandler, J.H., 1997. Digital photogrammetric monitoring
749 of river bank erosion. *The Photogrammetric Record* 15, 753-764.

750 Remondino, F., El-Hakim, S., 2006. Image-based 3-D modelling: a review. *The*
751 *Photogrammetric Record* 21, 269-291.

752 Remondino, F., Fraser, C. 2006. The International Archives of the Photogrammetry
753 and Remote Sensing Commission V Symposium 'Image Engineering and Vision
754 Metrology', 266-272.

755 Richardson, S.D., Reynolds, J.M., 2000. An overview of glacial hazards in the
756 Himalayas. *Quaternary International* 65/66: 31-47.

757 Rieke-Zapp, D.H., Nearing, M.A., 2005. Digital close range photogrammetry for
758 measurement of soil erosion. *The Photogrammetric Record* 20, 69-87.

759 Rosser, N.J., Petley, D.N., Lim, M., Dunning, S.A., Allison, R.J., 2005. Terrestrial
760 laser scanning for monitoring the process of hard rock coastal cliff erosion. *Quarterly*
761 *Journal of Engineering Geology and Hydrogeology* 38, 363-375.

762 Rychkov, I., Brasington, J., Vericat, D., 2012. Computational and methodological
763 aspects of terrestrial surface analysis based on point clouds. *Computers &*
764 *Geosciences* 42, 64-70.

765 Sacchetti, F., Benetti, S., Georgiopoulou, A., Shannon, P.M., O'Reilly, B.M. Dunlop,
766 P., Quinn, R., Cofaigh, C.O., 2012. Deep-water geomorphology of the glaciated Irish
767 margin from high-resolution marine geophysical data. *Marine Geology* 291, 113-131.

768 Sahlin, E., Glasser, N.F., 2008. Geomorphological map of Cadair Idris, Wales.
769 *Journal of Maps* 6: 299-314.

770 Smith, M., Chandler, J., Rose, J., 2009. High spatial resolution data acquisition for
771 the geosciences: kite aerial photography. *Earth Surface Processes and Landforms*
772 34: 155-161.

773 Snavely, N., 2008. Scene Reconstruction and Visualization from Internet Photo
774 Collections, unpublished PhD thesis, University of Washington, USA.

775 Snavely, N., Seitz, S.N., Szeliski, R., 2006. Photo Tourism: Exploring image
776 collections in 3D, *ACM Transactions on Graphics*, New York, pp. 1-12.

777 Snavely, N., Seitz, S.N., Szeliski, R., 2008. Modeling the world from internet photo
778 collections. *International Journal of Computer Vision* 80: 189-210. Spetsakis, M.E.,
779 Aloimonos, Y., 1991. A multi-frame approach to visual motion perception.
780 *International Journal of Computer Vision* 6: 245-255.

781 Stojic, M., Chandler, J.H., Ashmore, P., Luce, J., 1998. The assessment of sediment
782 transport rates by automated digital photogrammetry. *Photogrammetric Engineering*
783 *and Remote Sensing* 64, 387-395.

784 Sturznegger, M., Stead, D., 2009. Close-range terrestrial digital photogrammetry and
785 terrestrial laser scanning for discontinuity characterization on rock cuts. *Engineering*
786 *Geology* 106, 163-182.

787 Szeliski, R., Kang, S.B., 1994. Recovering 3-D shape and motion from image
788 streams using nonlinear least squares. *Journal of Visual Communication and Image*
789 *Representation* 5: 10-28.

790 Vericat, D., Brasington, J., Wheaton, J., Cowie, M., 2009. Accuracy assessment of
791 aerial photographs acquiring using lighter-than-air blimps: low cost tools for mapping
792 river corridors. *River Research and Applications* 25: 985-1000.

793 Vuichard, D., Zimmerman, M., 1986. The Langmoche flash-flood, Khumbu Himal,
794 Nepal. *Mountain Research and Development* 6: 90-94.

795 Vuichard, D., Zimmerman, M., 1987. The 1985 catastrophic drainage of a moraine-
796 dammed lake, Khumbu Himal, Nepal: cause and consequences. *Mountain Research*
797 *and Development* 7: 91-110.

798 Westaway, R.M., Lane, S.N., Hicks, D.M., 2000. The development of an automated
799 correction procedure for digital photogrammetry for the study of wide, shallow,
800 gravel-bed rivers. *Earth Surface Processes and Landforms* 25, 209-226.

801 Wolf, P.R., Dewitt, B.A., 2000. *Elements of Photogrammetry with Applications in GIS*
802 (3rd edition), McGraw-Hill, Boston.

803

804 Fig. captions:

805

806 **Table 1.** Processing batch description and SfM output for Constitution Hill, Dig Tsho, and
807 Cwm Cau.

808

809 **Table 2.** GCP positional accuracies and transformation residuals (Dig Tsho and Cwm Cau
810 only). TLS system position taken as true for transformation of Constitution Hill SfM data.

811

812 **Fig. 1.** Instead of a single stereo pair, the SfM technique requires multiple, overlapping
813 photographs as input to feature extraction and 3-D reconstruction algorithms.

814

815 **Fig. 2.** Lowe's (2004) Scale Invariant Feature Transform (SIFT) algorithm decomposes a
816 given image (left) into a database of 'keypoint descriptors' (right). Lines represent individual
817 keypoints, proportionally scaled according to the radius of the image region (pixels)
818 containing the keypoint (SIFT code available: <http://www.cs.ubc.ca/~lowe/keypoints/>).

819

820 **Fig. 3.** From photograph to point-cloud: the Structure-from-Motion workflow.

821

822 **Fig. 4.** Constitution Hill, Aberystwyth. (a) Aerial perspective of the site. Area reconstructed
823 using SfM and TLS is highlighted in red, GCP positions are shown in yellow, and TLS
824 position are shown in blue. Inset map shows relative location of Constitution Hill (CH), and
825 Cwm Cau (CC). Imagery georeferenced to UTM Zone 30N coordinate system. (b) 1 m²
826 tarpaulin squares were used as GCPs on Constitution Hill. Centroid positions were recorded
827 using dGPS. (c) A GCP target, as it appears in a photograph, and; (d) as represented in the
828 dense point cloud.

829

830 **Fig. 5.** Perspective views of Constitution Hill. (a) Panorama of the survey area (with GCPs
831 clearly visible), and; reconstructed (b) sparse and (c) dense point clouds. See text for
832 description of A, B, and C in (a).

833

834 **Fig. 6.** Exposed oblique section of a fold in Silurian turbidites at the base of Constitution Hill
835 as captured in (a) an input photograph, and as resolved (b) in the dense point cloud.
836 Prominent (lighter) layers are sandstone, softer (darker) layers are mudstone. See
837 annotation 'C' in Fig. 5 for location.

838

839 **Fig. 7.** Final interpolated DEMs of Constitution Hill using (a) TLS and (b) SfM data; (c) aerial
840 photograph of the site; (d) point density map. **A** and **B** refer to associated labels in Fig. 5a.
841 **VF** and **DV** refer to, respectively, vegetation-free and densely vegetated sub-regions
842 analysed in Fig. 10. Data georeferenced to UTM Zone 30N coordinate system.

843

844 **Fig. 8.** Per-cell point density frequency distribution plots for: (a) Constitution Hill SfM DEM;
845 (b) Constitution Hill TLS DEM; (c) Dig Tsho SfM DEM (note: upper limit of x axis manually
846 truncated at 150 points per m² to preserve histogram form; refer to Fig. 12b for complete
847 range of density values); (d) Cwm Cau SfM DEM..

848 **Fig. 9.** DEM of difference results (TLS – SfM). (a) Spatial representation of the Z_{diff} frequency
849 distribution. Data georeferenced to UTM Zone 30N coordinate system. (b) Z_{diff} frequency
850 distribution. **A**: the headwall at the highest point of the surveyed area; **B**: near-vertical cliffs;
851 **C**: dense vegetation cover; **D**: interpolation error.

852

853 **Fig. 10.** Local scale (20 m²) Z_{diff} frequency distribution data for an area with (a) dense
854 vegetation cover, and (b) vegetation-free. As anticipated, elevation differences in the
855 absence of vegetation are considerably lower.

856

857 **Fig. 11.** Dig Tsho glacial lake. **(a)** View towards the terminal moraine complex at Dig Tsho,
858 Khumbu Himal, Nepal. A large breach, produced by a Glacial Lake Outburst Flood is clearly
859 identifiable to the right of the photograph; **(b)** the spatial extent of SfM reconstruction. GCP
860 locations also shown. (photo: M Westoby).

861

862 **Fig. 12.** Dig Tsho SfM data products. (a) Oblique view of the final hill-shaded model of Dig
863 Tsho. Clearly identifiable morphological features include the 1985 breach, as well as two
864 abandoned spillways (AS) which cross the terminal moraine. Current lake extent shown for
865 reference. The up-valley end of the lake has not been fully reconstructed, resulting in
866 interpolation artefacts; (b) oblique view showing per-cell (1 m²) point densities. Data
867 transformed to UTM Zone 45N geographic coordinate system.

868

869 **Fig. 13.** Glacially-sculpted bedrock ridge, Cwm Cau, Snowdonia. (a) Photograph of the
870 southern face of the feature; (b) hill-shaded DEM, demonstrating the capability of the SfM
871 data to resolve small scale (cm) features.

872

873 **Fig. 14.** Oblique, hill-shaded views of the final SfM DEM Cwm Cau bedrock ridge, showing:
874 (a) the south and (b) north faces. Areas of low point density resulted in extensive
875 interpolation across elevated sections. Data transformed to UK Ordnance Survey National
876 Grid coordinate system (OSGB36 datum).

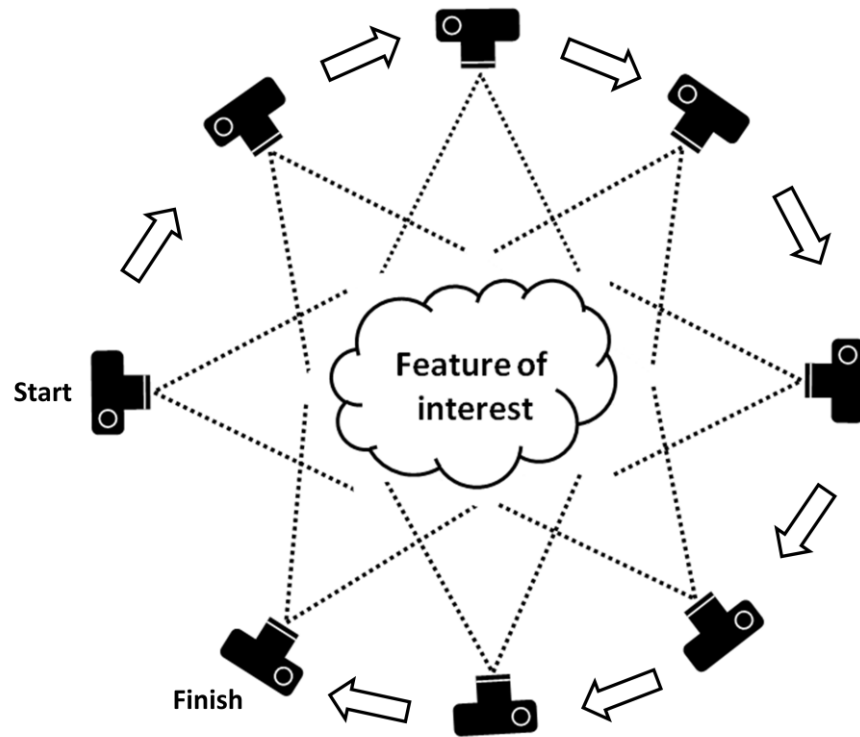


Fig. 1. Instead of a single stereo pair, the SfM technique requires multiple, overlapping photographs as input to feature extraction and 3D reconstruction algorithms.

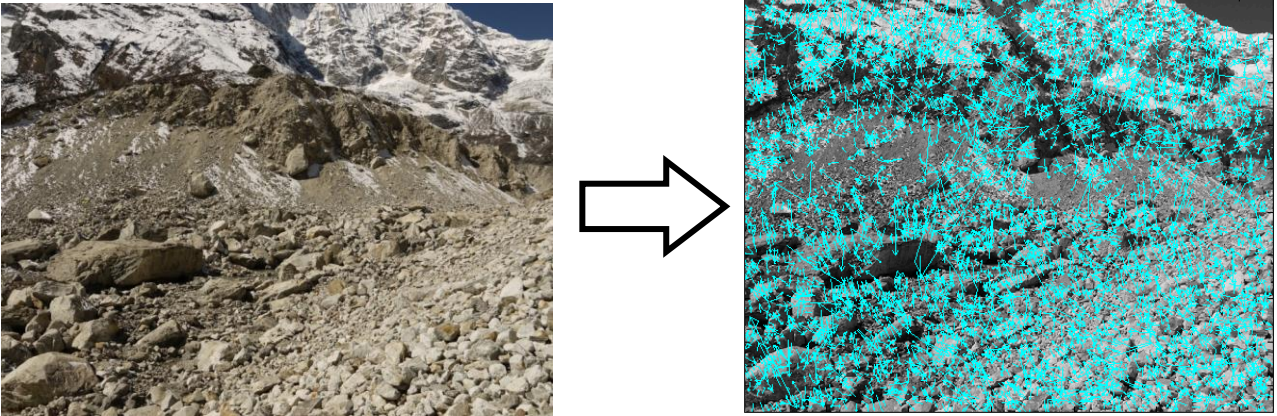


Fig. 2. Lowe's (2004) Scale Invariant Feature Transform (SIFT) algorithm decomposes a given image (left) into a database of 'keypoint descriptors' (right). Lines represent individual keypoints, proportionally scaled according to the radius of the image region (pixels) containing the keypoint (SIFT code available: <http://www.cs.ubc.ca/~lowe/keypoints/>)

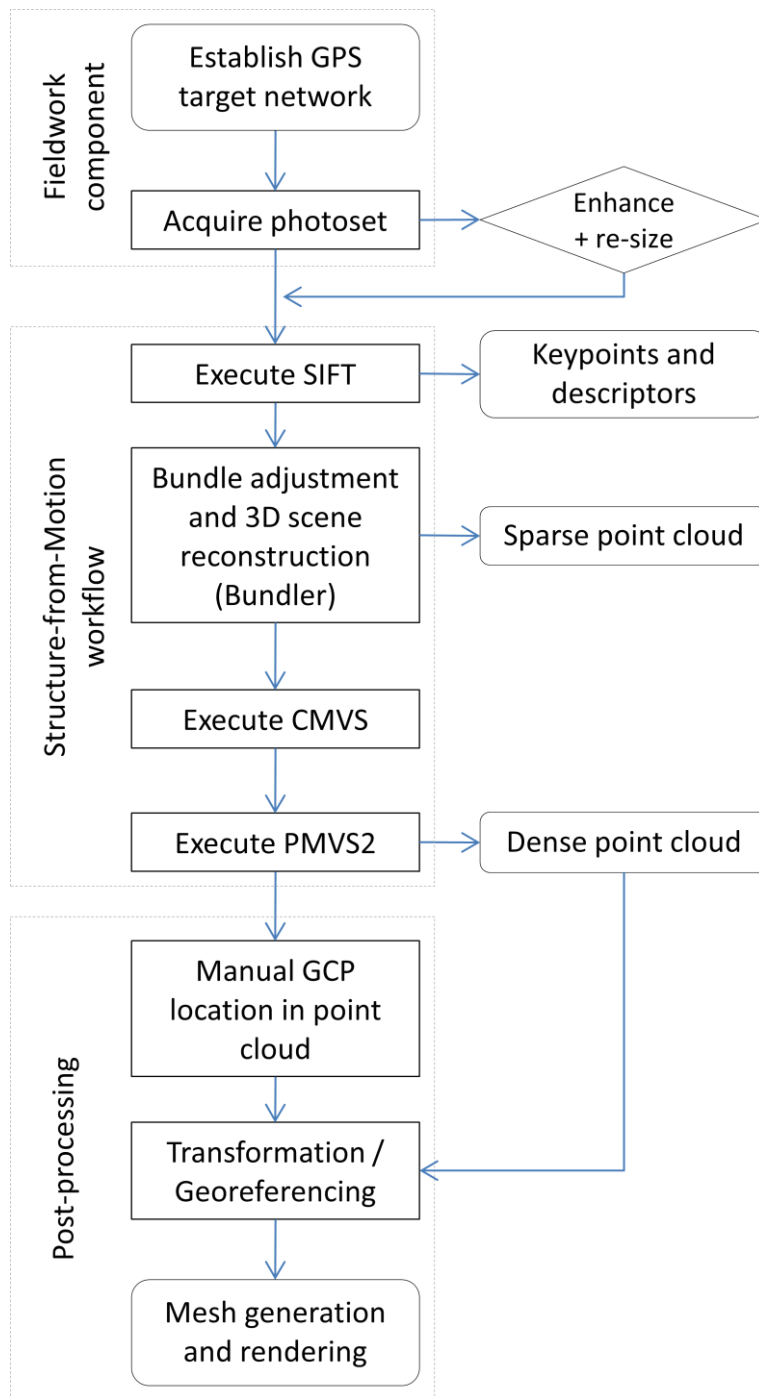


Fig. 3. From photograph to point-cloud: the Structure-from-Motion workflow.

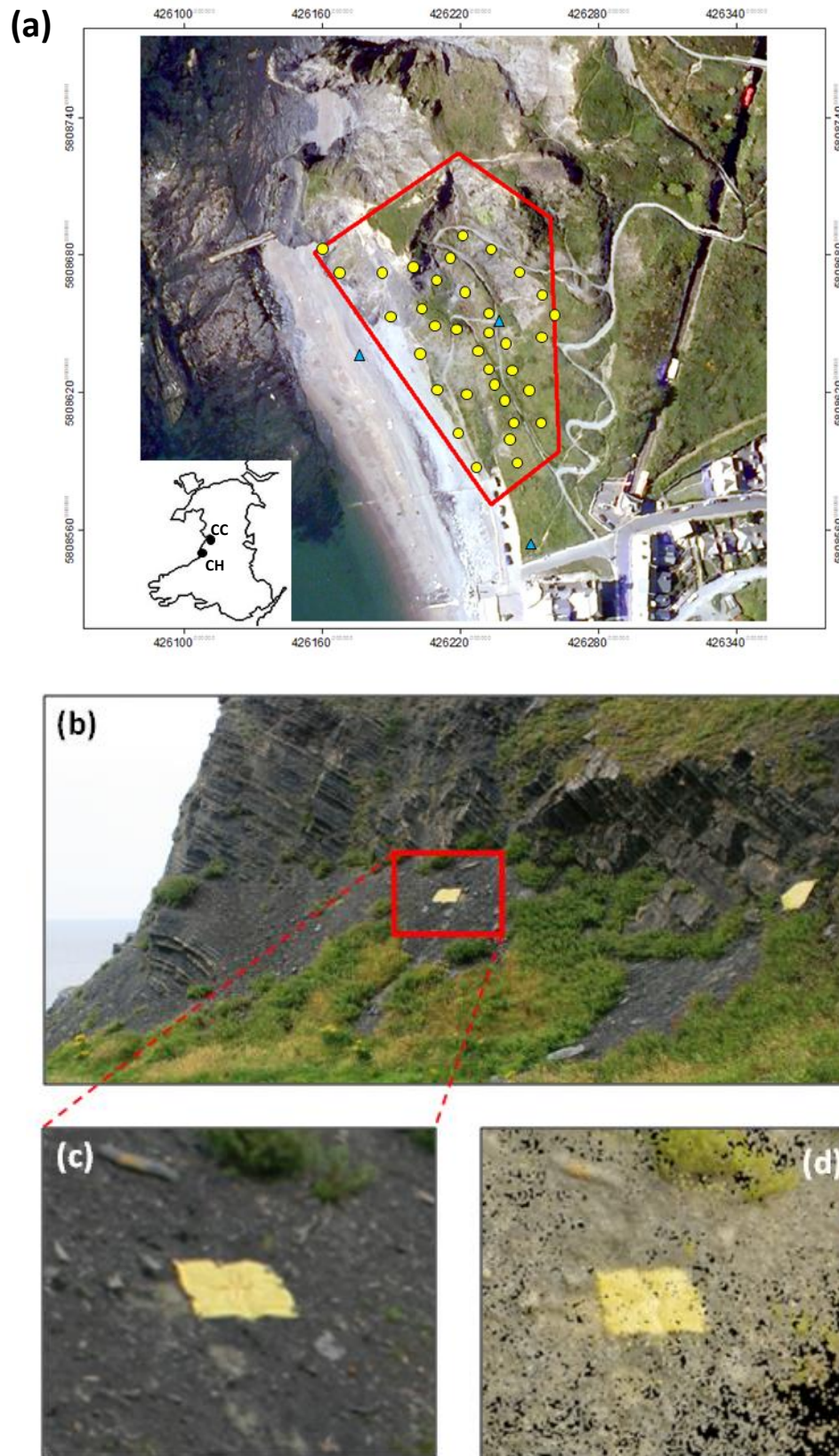


Fig. 4. Constitution Hill, Aberystwyth. (a) Aerial perspective of the site. Area reconstructed using SfM and TLS is highlighted in red, GCP positions are shown in yellow, and TLS position are shown in blue. Inset map shows relative location of Constitution Hill (CH), and Cwm Cau (CC). Imagery georeferenced to UTM Zone 30N coordinate system. (b) 1 m² tarpaulin squares were used as GCPs on Constitution Hill. Centroid positions were recorded using dGPS. (c) A GCP target, as it appears in a photograph, and; (d) as represented in the dense point cloud.

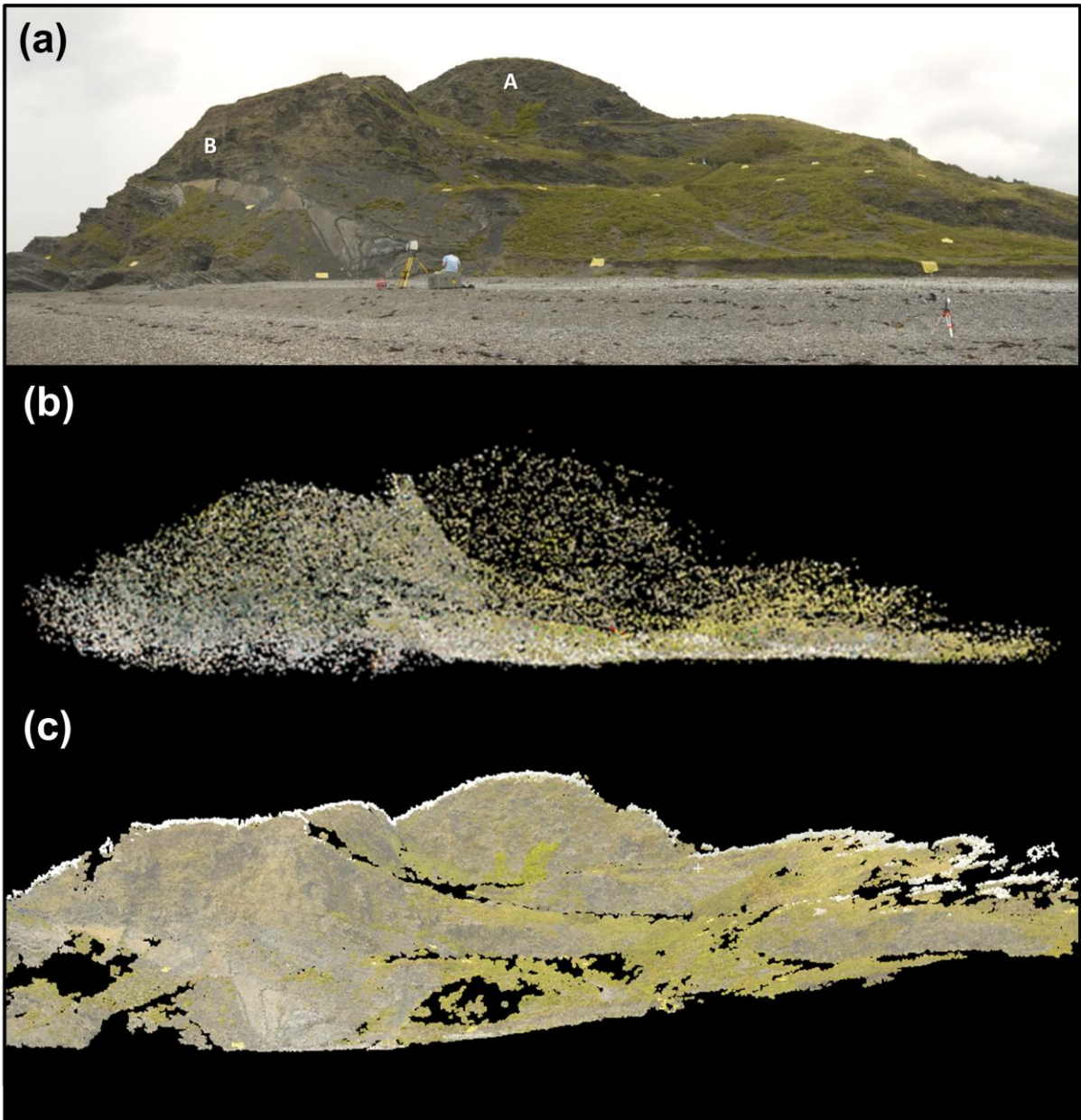


Fig. 5. Perspective views of Constitution Hill. (a) Panorama of the survey area (with GCPs clearly visible), and; reconstructed (b) sparse and (c) dense point clouds. See text for description of A and B in (a).

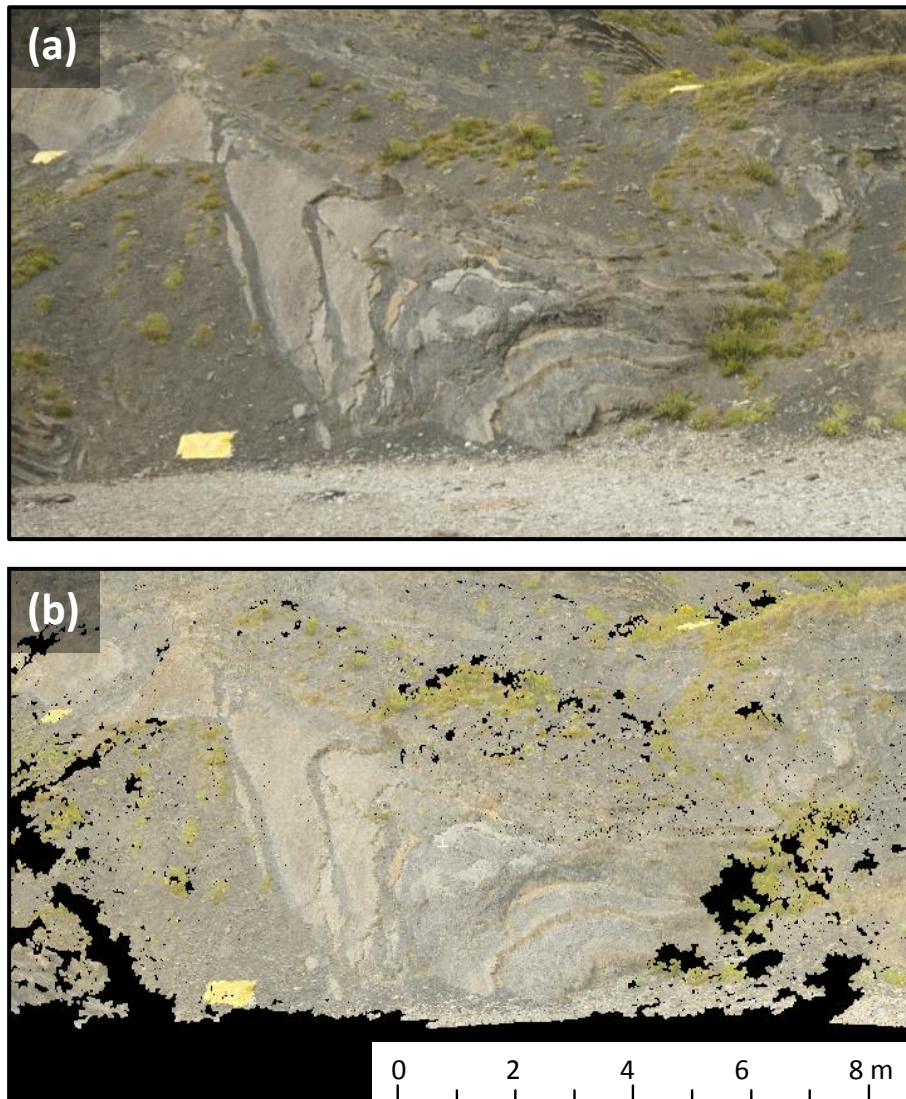


Fig. 6. Exposed oblique section of a fold in Silurian turbidites at the base of Constitution Hill as captured in (a) an input photograph, and as resolved (b) in the dense point cloud. Prominent (lighter) layers are sandstone, softer (darker) layers are mudstone. See annotation 'C' in Fig. 5 for location.

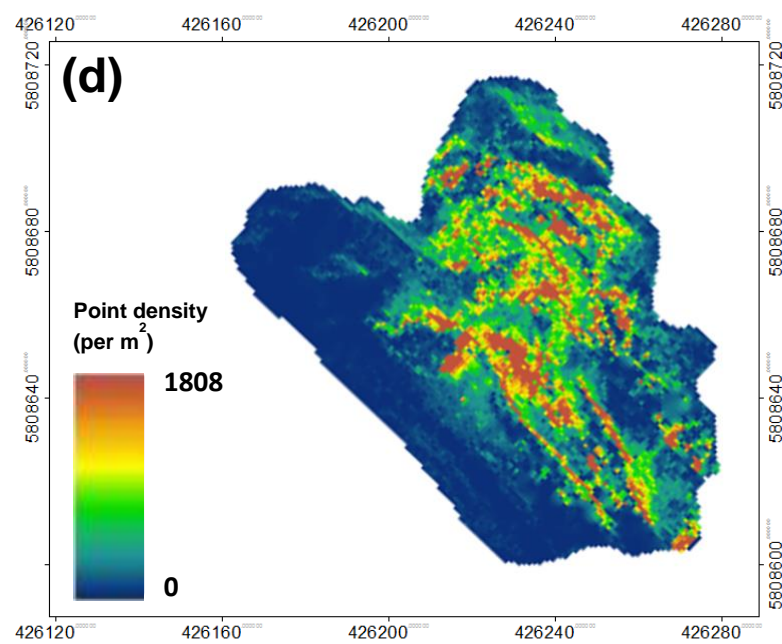
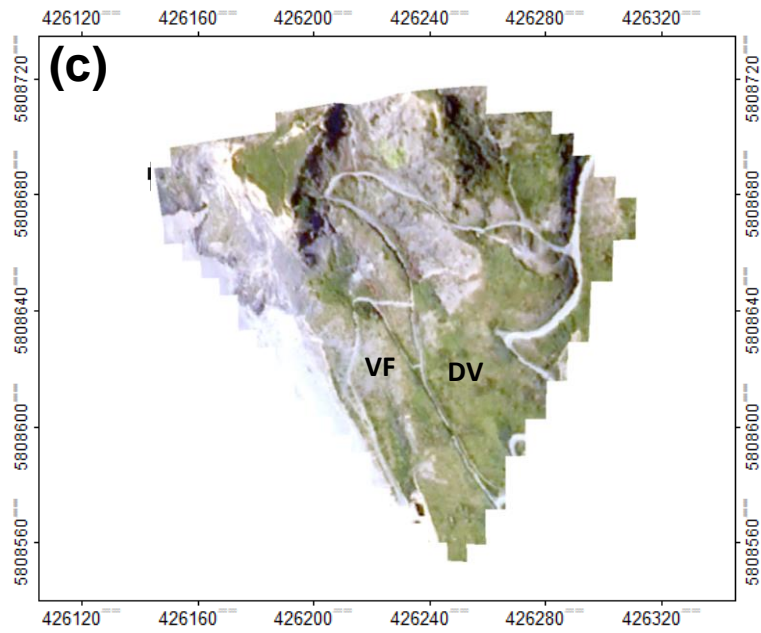
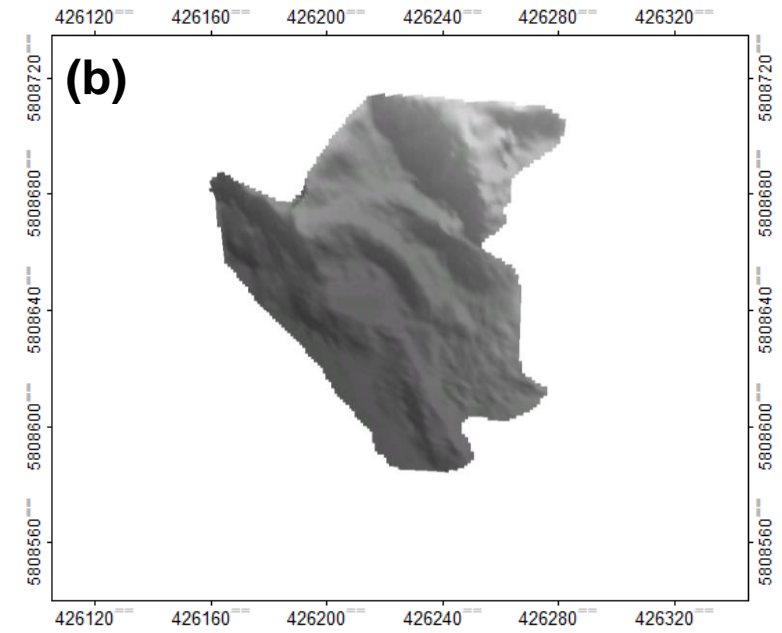
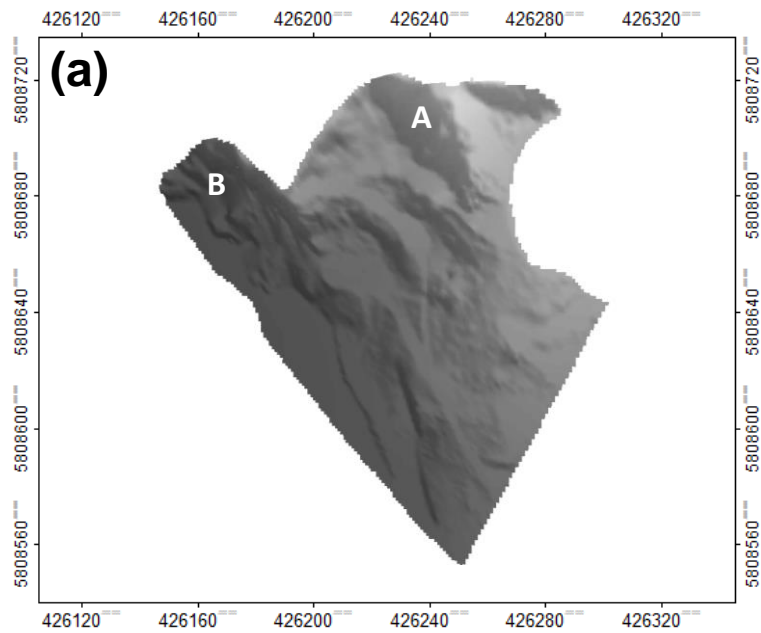


Fig. 7. Final interpolated DEMs of Constitution Hill using (a) TLS and (b) SfM data; (c) aerial photograph of the site; (d) point density map. **A** and **B** refer to associated labels in Fig. 5a. **VF** and **DV** refer to, respectively, vegetation-free and densely vegetated sub-regions analysed in Fig. 10. Data georeferenced to UTM Zone 30N coordinate system.

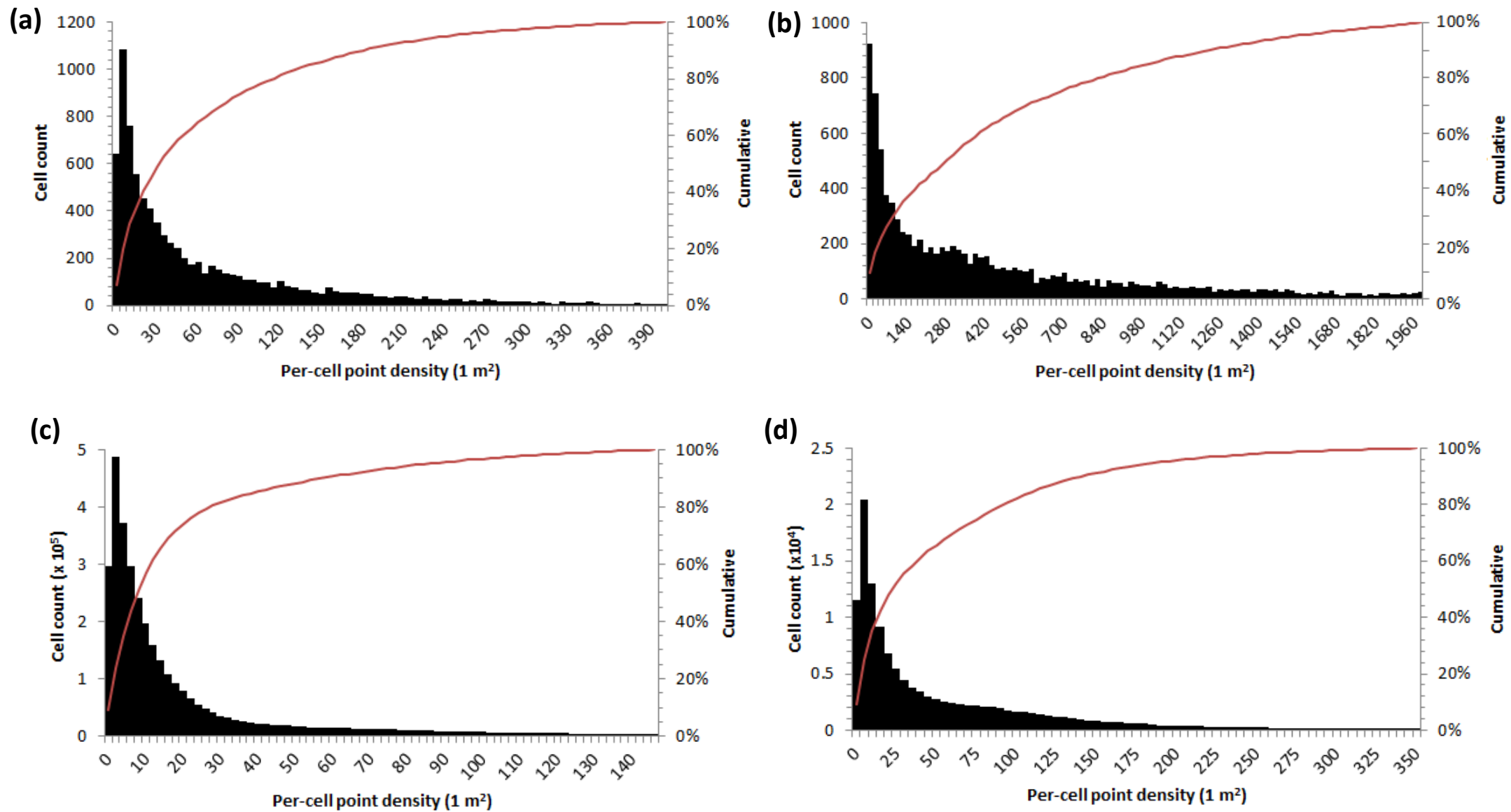


Fig. 8. Per-cell point density frequency distribution plots for: (a) Constitution Hill SfM DEM; (b) Constitution Hill TLS DEM; (c) Dig Tsho SfM DEM (note: upper limit of x axis manually truncated at 150 points per m² to preserve histogram form; refer to Fig. 12b for complete range of density values); (d) Cwm Cau SfM DEM.

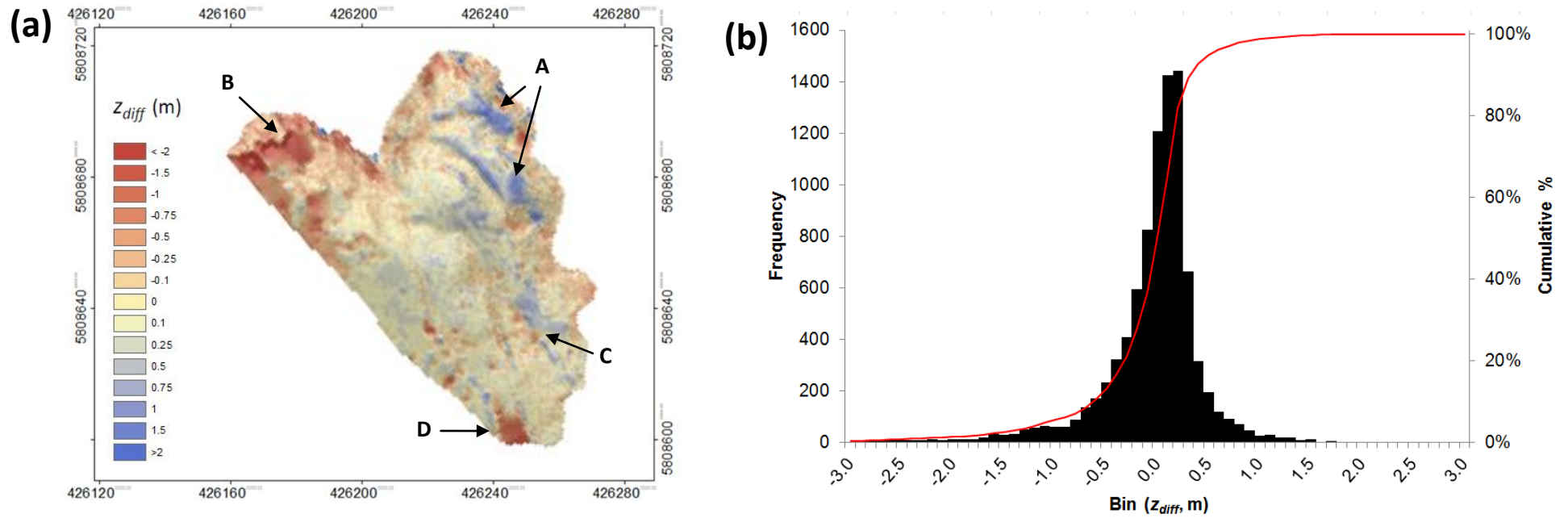


Fig. 9. DEM of difference results (TLS – SfM). (a) Spatial representation of the z_{diff} frequency distribution. Data georeferenced to UTM Zone 30N coordinate system. (b) z_{diff} frequency distribution. **A:** the headwall at the highest point of the surveyed area; **B:** near-vertical cliffs; **C:** dense vegetation cover; **D:** interpolation error.

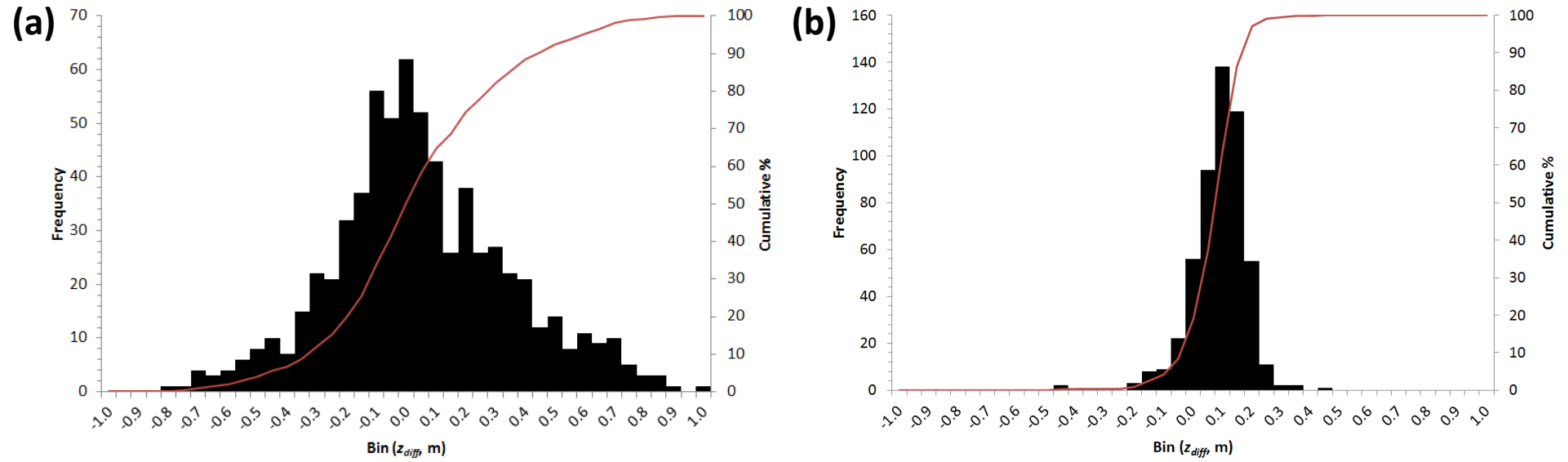


Fig. 10. Local scale (20 m²) z_{diff} frequency distribution data for an area with (a) dense vegetation cover, and (b) vegetation-free. As anticipated, elevation differences in the absence of vegetation are considerably lower. See **DV** and **VF** in Fig. 7 for locations.

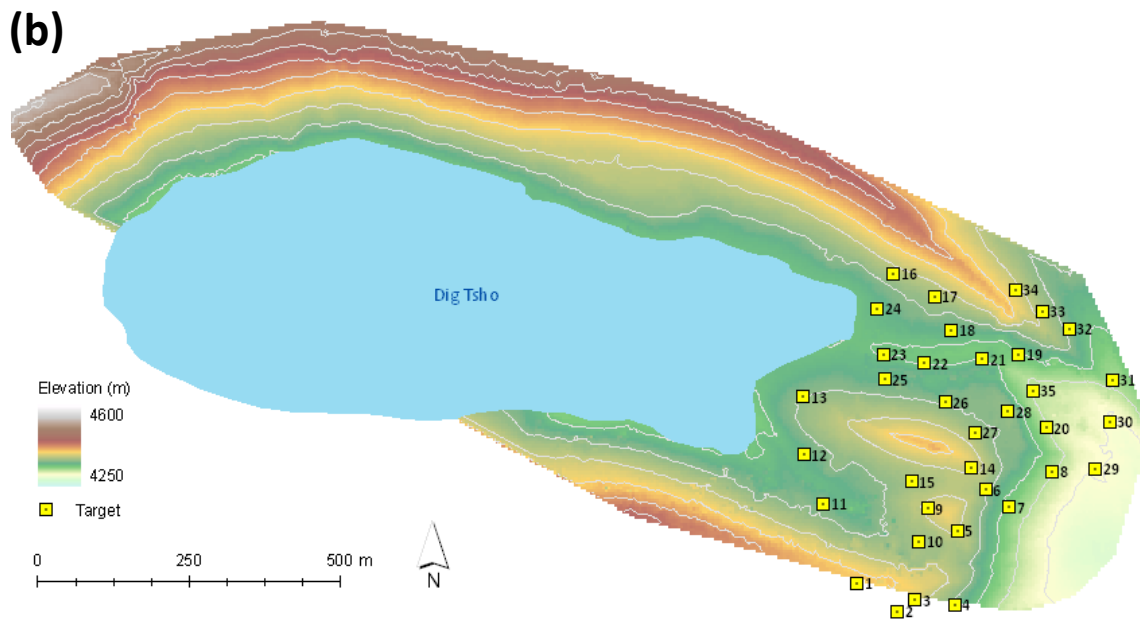
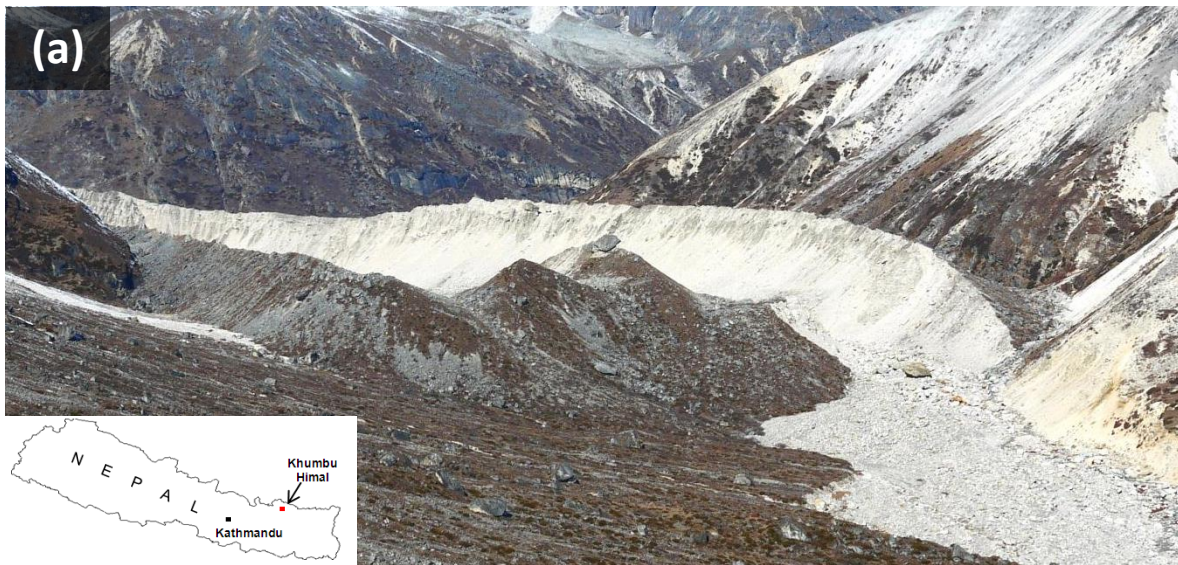


Fig. 11. Dig Tsho glacial lake. **(a)** View towards the terminal moraine complex at Dig Tsho, Khumbu Himal, Nepal. A large breach, produced by a Glacial Lake Outburst Flood is clearly identifiable to the right of the photograph; **(b)** the spatial extent of SfM reconstruction. GCP locations also shown. (photo: M Westoby).

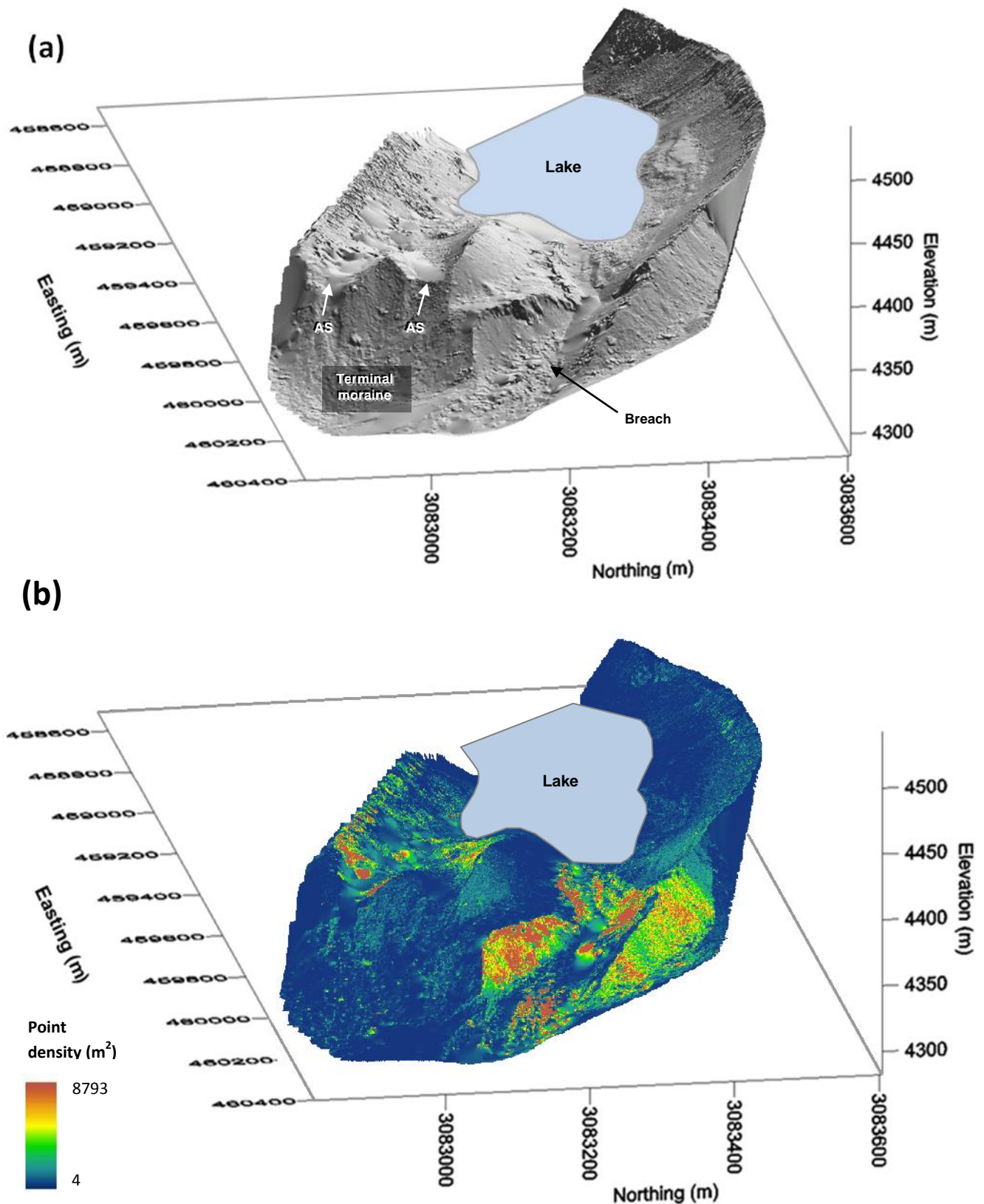


Fig. 12. Dig Tsho SfM data products. (a) Oblique view of the final hill-shaded model of Dig Tsho. Clearly identifiable morphological features include the 1985 breach, as well as two abandoned spillways (AS) which cross the terminal moraine. Current lake extent shown for reference. The up-valley end of the lake has not been fully reconstructed, resulting in interpolation artefacts; (b) oblique view showing per-cell (1 m^2) point densities. Data transformed to UTM Zone 45N geographic coordinate system.



Fig. 13. Glacially-sculpted bedrock ridge, Cwm Cau, Snowdonia. (a) Photograph of the southern face of the feature; (b) hill-shaded DEM, demonstrating the capability of the SfM data to resolve small scale (cm) features.

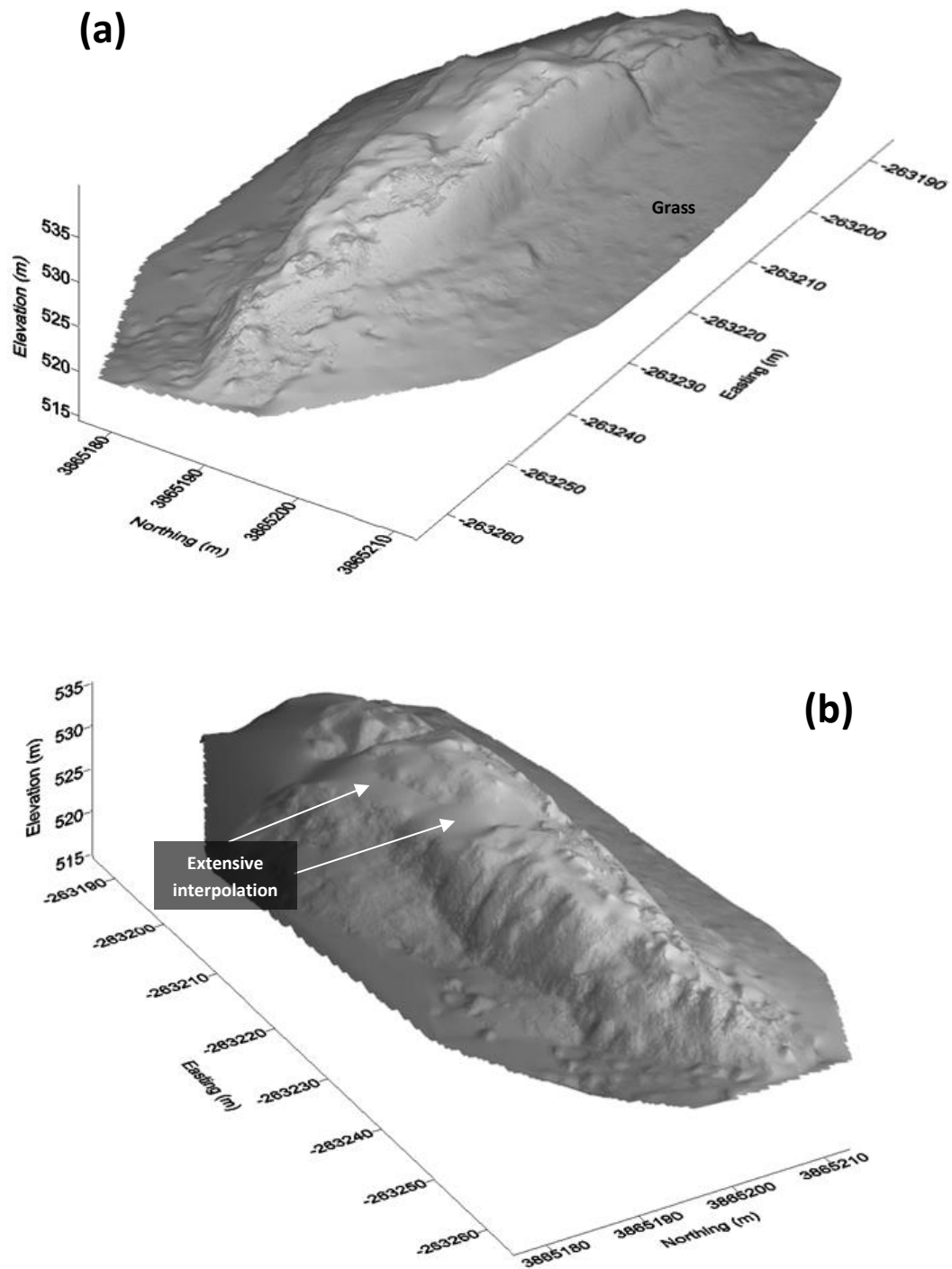


Fig. 14. Oblique, hill-shaded views of the final SfM DEM Cwm Cau bedrock ridge, showing: (a) the south and (b) north faces. Areas of low point density resulted in extensive interpolation across elevated sections. Data transformed to UK Ordnance Survey National Grid coordinate system (OSGB36 datum).

Table 2. Processing batch description and SfM output for Constitution Hill, Dig Tsho, and Cwm Cau.

Site / batch	No. of photos	Sparse points	Dense points
<i>Constitution Hill</i>			
CH_Ba1	159	5.8×10^4	2.9×10^6
CH_Ba2	411	8.2×10^4	5.8×10^6
CH_Ba3	286	3.8×10^4	2.7×10^6
<i>Dig Tsho</i>			
DT_Ba1	457	6.1×10^4	4.3×10^6
DT_Ba2	560	7.2×10^4	1.0×10^7
DT_Ba3	609	9.1×10^4	8.3×10^6
<i>Cwm Cau</i>			
CC_Ba1	264	7.0×10^4	5.1×10^6
CC_Ba2	536	1.2×10^5	7.3×10^6

Table 1. GCP positional accuracies and transformation residuals (Dig Tsho and Cwm Cau only). TLS system position taken as true for transformation of Constitution Hill SfM data.

Site	Ground-truth or GCP uncertainty (m; mean)			Batch	Transformation residuals (m)		
	x + y	z	xyz		x	y	z
Constitution Hill (Wales)	-	-	-	CC_Ba1	0.196	0.156	0.020
				CC_Ba2	0.076	0.064	0.035
				CC_Ba3	0.016	0.072	0.005
Dig Tsho (Nepal)	0.110	0.195	0.226	DT_Ba1	1.022	1.158	2.917
				DT_Ba2	0.630	0.694	3.241
				DT_Ba3	1.015	0.482	4.653
Cwm Cau (Wales)	0.002	0.002	0.003	CC_Ba1	0.538	0.117	0.164
				CC_Ba2	1.411	0.205	0.679